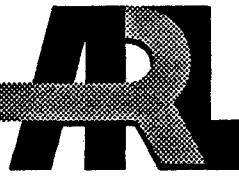


ARMY RESEARCH LABORATORY

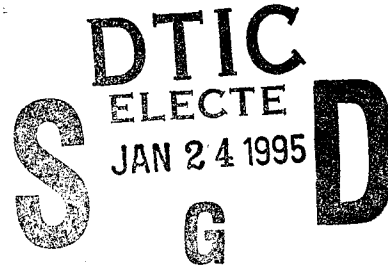


Oblique Impact Modeling of Fuzes

George A. Gazonas
Steven B. Segletes
Vincent M. Boyle
Steven R. Stegall

ARL-TR-665

January 1995



DTIC QUALITY INSPECTED 3

APPROVED FOR PUBLIC RELEASE; DISTRIBUTION IS UNLIMITED.

19950120 021

NOTICES

Destroy this report when it is no longer needed. DO NOT return it to the originator.

Additional copies of this report may be obtained from the National Technical Information Service, U.S. Department of Commerce, 5285 Port Royal Road, Springfield, VA 22161.

The findings of this report are not to be construed as an official Department of the Army position, unless so designated by other authorized documents.

The use of trade names or manufacturers' names in this report does not constitute endorsement of any commercial product.

REPORT DOCUMENTATION PAGE

Form Approved
OMB No. 0704-0188

Public reporting burden for this collection of information is estimated to average 1 hour per response, including the time for reviewing instructions, searching existing data sources, gathering and maintaining the data needed, and completing and reviewing the collection of information. Send comments regarding this burden estimate or any other aspect of this collection of information, including suggestions for reducing this burden, to Washington Headquarters Services, Directorate for Information Operations and Reports, 1215 Jefferson Davis Highway, Suite 1204, Arlington, VA 22202-4302, and to the Office of Management and Budget, Paperwork Reduction Project (0704-0188), Washington, DC 20503.

1. AGENCY USE ONLY (Leave blank)	2. REPORT DATE	3. REPORT TYPE AND DATES COVERED
	January 1995	Final, Oct 93 - Dec 93
4. TITLE AND SUBTITLE		5. FUNDING NUMBERS
Oblique Impact Modeling of Fuzes		WO: 4G015-414-R4
6. AUTHOR(S)		
George A. Gazonas, Steven B. Segletes, Vincent M. Boyle, and Steven R. Stegall		
7. PERFORMING ORGANIZATION NAME(S) AND ADDRESS(ES)		8. PERFORMING ORGANIZATION REPORT NUMBER
U.S. Army Research Laboratory ATTN: AMSRL-WT-PD Aberdeen Proving Ground, MD 21005-5066		
9. SPONSORING/MONITORING AGENCY NAMES(S) AND ADDRESS(ES)		10. SPONSORING/MONITORING AGENCY REPORT NUMBER
U.S. Army Research Laboratory ATTN: AMSRL-OP-AP-L Aberdeen Proving Ground, MD 21005-5066		ARL-TR-665
11. SUPPLEMENTARY NOTES		
12a. DISTRIBUTION/AVAILABILITY STATEMENT		12b. DISTRIBUTION CODE
Approved for public release; distribution is unlimited.		
13. ABSTRACT (Maximum 200 words)		
<p>This report presents the results of a combined experimental, numerical, and analytical investigation of a low-speed (198 m/s) oblique impact of a cylindrical steel projectile into an aluminum-brass composite fuze simulant. The numerical simulations were performed prior to the experiments using the Lagrangian hydrocode EPIC92. The results indicate that projectile hardness and impact point strongly influence the mechanism by which the fuze deforms. An experiment was then conducted in order to evaluate the predictive capabilities of the hydrocode. The experimental results generally corroborate the hydrocode results during the initial stages of the impact but depart significantly at later stages of the penetration. Possible causes for the observed differences between the experiment and the simulation include: 1) the absence of a global fracture modeling capability in the hydrocode, and 2) boundary condition differences between experiment and simulation. The hydrocode predicts that 91% of the projectile kinetic energy is converted into target plastic work. This result compares well with predictions based upon an analytical model of an elastic-plastic beam bent by an end load.</p>		
14. SUBJECT TERMS		15. NUMBER OF PAGES
impact, render safe, kinetic energy projectiles, fuzes, hydrocode simulation		49
		16. PRICE CODE
17. SECURITY CLASSIFICATION OF REPORT	18. SECURITY CLASSIFICATION OF THIS PAGE	19. SECURITY CLASSIFICATION OF ABSTRACT
UNCLASSIFIED	UNCLASSIFIED	UNCLASSIFIED
NSN 7540-01-280-5500		20. LIMITATION OF ABSTRACT
		UL

INTENTIONALLY LEFT BLANK.

ACKNOWLEDGMENT

This work was supported by the Naval Explosive Ordnance Disposal (NAVEOD) Technology Center, Indian Head, Maryland, under Army Research Laboratory (ARL) work order number 4G015-414-R4. The authors would like to acknowledge the overall assistance of Mr. Atul Patel of NAVEOD with regard to the fuze render-safe problem. Appreciation is also expressed to Mr. Rich Gold of NAVEOD for expedient delivery of the projectile and fuze simulant used in the field test. Thanks also go to Mr. Todd Bjerke and Dr. Ken Bannister for their constructive reviews.

Accesion For	
NTIS	CRA&I
DTIC	TAB
Unannounced	
Justification _____	
By _____	
Distribution / _____	
Availability Codes	
Dist	Avail and / or Special
A-1	

INTENTIONALLY LEFT BLANK.

TABLE OF CONTENTS

	<u>Page</u>
ACKNOWLEDGMENT.....	iii
LIST OF FIGURES.....	vii
1. INTRODUCTION.....	1
2. PROBLEM DESCRIPTION.....	2
3. NUMERICAL APPROACH.....	3
3.1 Geometry.....	3
3.2 Boundary Conditions.....	4
3.3 Constitutive Equations.....	4
3.4 Damage and Erosion Criteria.....	6
4. NUMERICAL RESULTS.....	6
4.1 Event 1. "Soft" Projectile, High-Impact Point.....	7
4.2 Event 2. "Hard" Projectile, High-Impact Point.....	7
4.3. Event 3. "Hard" Projectile, Low-Impact Point.....	8
5. IMPACT EXPERIMENTS.....	9
6. COMPARISON OF NUMERICAL AND EXPERIMENTAL RESULTS.....	9
7. ANALYTICAL APPROACH.....	11
7.1 Deflections of a Cantilever Beam.....	12
7.2 Elastic-Plastic Deflections of a Cantilever Beam.....	13
7.3 Complementary Energy of an Elastic-Plastic Cantilever Beam.....	16
8. COMPARISON OF NUMERICAL AND ANALYTICAL RESULTS.....	17
9. CONCLUSIONS.....	20
10. REFERENCES.....	35

	<u>Page</u>
LIST OF SYMBOLS.....	37
DISTRIBUTION LIST.....	39

LIST OF FIGURES

<u>Figure</u>	<u>Page</u>
1. Cutaway View of a Typical Fuze, Illustrating Internal Components..	23
2. Fuze and Projectile Boundary Conditions (dimensions in meters).....	23
3. Adiabatic Flow Stress Versus Equivalent Plastic Strain Curves as a Function of Strain Rate for Gun Cartridge Brass, 6061-T6 Aluminum and 4340 and Modified S-7 Tool Steels.....	24
4. Finite Element Mesh Used in Numerical Simulations.....	25
5. Event 1. "Soft" High-Impact EPIC92 Hydrocode Results.....	25
6. Event 2. "Hard" High-Impact EPIC92 Hydrocode Results.....	26
7. Event 3. "Hard" Low-Impact EPIC92 Hydrocode Results.....	27
8. $\dot{\epsilon}^p = 0.20$ Contours for "Hard" Projectile Impacts a) Event 2, b) Event 3.....	28
9. Ballistic Range Configuration.....	29
10. X-Ray Radiograph of Impact Event at 272 μ s and EPIC92 Hydrocode Simulation Overlay at 280 μ s.....	30
11. Photograph of Damaged Fuze Simulant Showing Severed Fuze Top with Circular Imprint of Projectile.....	30
12. Modeling Simplifications a) Simplified Fuze Geometry (Prismatic Circular Cantilever Beam), b) Beam Cross Section Showing Integration Coordinate System and Regions of Elastic and Plastic Behavior, c) Elastic-Perfectly Plastic Material Model.....	31
13. Moment Versus Curvature Relationship for an Elastic-Plastic Cantilever Beam.....	31
14. Moment Versus Curvature Plots for an Elastic-Plastic Cantilever Beam of Circular Cross Section.....	32
15. Load Versus Deflection (Eqn. 24) for an Elastic-Plastic Cantilever Beam of Circular Cross Section.....	32

LIST OF FIGURES (continued)

<u>Figure</u>		<u>Page</u>
16.	Fuze Centerline Distortion (in meters) Versus Time for Event 2.....	33
17.	Equivalent Plastic Strain Contours at 120 μ s, Showing Fully Developed Plasticity Across the Diameter of the Fuze.....	33

1. INTRODUCTION

There are a number of munition-related problems of interest to the defense community in which the presence of energetic materials is integral. One such area of investigation is that of explosive ordnance disposal (EOD) render-safe procedures, in which a potentially armed and thus dangerous fuze is disabled in situ, in order to render it safe for subsequent handling and removal. One class of render-safe methods might be termed "mechanical," in that it relies on a measured use of mechanical force to sever or disrupt the explosive initiation train within the fuze.

One such mechanical technique to render a fuze safe is to impact it with a hardened projectile at an oblique angle, for example, perpendicular to the fuze's axis of symmetry. With the proper selection of impact location and speed, the mechanical damage induced by the impact can be made sufficiently brisant to isolate the high-explosive primer material from subsequent stages of the high-explosive train. However, the impact should not shock the fuze to an extent which causes the explosive material to initiate. The EOD community currently employs this mechanical method in certain render-safe procedures.

The physical process of rendering a fuze safe in situ can be quite hazardous. In addition, certain types of foreign-made ordnance are of limited supply, and not available for parametric testing. For these reasons, it is recognized that numerical simulation may assist in the development of render-safe procedures. To this end, this report discusses an investigation into the suitability of employing the EPIC92 hydrocode in the modeling of an oblique fuze impact, a mechanical render-safe procedure. The corresponding experiment was performed after the simulation work was completed, which provides a direct comparison for the simulation results. Another advantage of conducting the impact experiment after the numerical analyses is in determining the best time to radiograph the fuze. Upon introducing the specifics of the idealized problem to be studied, the problem geometry, constitutive properties, and boundary conditions of the problem are described. The results of finite element numerical simulations and experiment are presented and compared. Finally, an elastic-plastic analytical solution is developed, which sheds insight into fuze render-safe mechanics, and is compared with the hydrocode results.

2. PROBLEM DESCRIPTION

Current work focuses on investigating the "structural" damage (i.e., the mechanical response) imparted to an inert fuze simulant as a result of an oblique impact, rather than establishing the impact conditions that are necessary to render safe an actual fuze device. Only after a proper understanding of the mechanical response is obtained may future work address the complete fuze render-safe problem by replacing the inert components of the fuze simulant with an explosive material. Hereafter, the fuze simulant will simply be referred to as the fuze.

A typical fuze geometry consists of a right-circular cone that threads into the ordnance at its base (Figure 1). The cutaway view also illustrates some of the important internal fuze components such as the firing pin, detonator, and booster. Although these components are critical for proper operation of the fuze under normal impact conditions, replacing the "fine" internal structure of the fuze with a homogeneous core material will simplify the oblique impact problem.

The fuze selected for analysis is comprised of an axially symmetric 6061-T6 aluminum sheath surrounding a softer brass core. The aluminum sheath is 2.40 in (61.0 mm) in diameter at the base, and tapers bilinearly from base to apex. The fuze height is 3.72 in (94.5 mm). The projectile consists of a solid, hard steel, right-circular cylinder, 1 in (25.4 mm) in diameter and 3 in (76.2 mm) long, with a mass of 300 g. It is designed to strike the fuze normal to its axis of symmetry during standard render-safe procedures. The initial configuration as modeled is shown in Figure 2, including a typical hit location and impact velocity. The specific engagement configurations for the three numerical simulations and single experiment were provided by Patel and Gold (1993) (see Sections 3.2 and 5).

It should be pointed out that in an actual oblique impact render-safe procedure, the barrel of the gun which launches the projectile is kept in close proximity to the target fuze. This actual configuration has the effect of providing lateral confinement on the projectile. However, both experiment and simulations are performed with a free-flying projectile, because a more proximate gun position might obscure the photographic coverage with propellant combustion products. This lack of lateral confine-

ment has two effects: it permits projectile rotation after impact, and it reduces the accuracy of the aim in the experiment.

3. NUMERICAL APPROACH

A number of hydrocodes (for example, CTH (McGlaun et al. 1987), SPH (Monaghan 1982), CALE (Tipton 1991), EPIC (Johnson 1977;1992a,b), MESA (Holian et al. 1991), HULL (Matuska 1984), and DYNA (Hallquist and Benson 1986)) are available to numerically simulate the render-safe impact event in question. The term "hydrocode" describes that class of continuum mechanics based numerical codes capable of solving wave propagation problems. This investigation uses the Lagrangian-based explicit EPIC92 (Elastic-Plastic Impact Calculations) hydrocode (Johnson et al. 1992a,b) because of: 1) previous impact modeling experience with EPIC92 and other similar Lagrangian-based hydrocodes (Segletes 1990), and 2) EPIC's capabilities for modeling ignition and detonation phenomena in explosive materials (Johnson et al. 1992a,b; Jones and Zerilli 1993). This explosive modeling capability will permit future efforts to model a more realistic fuze configuration while at the same time retain compatibility with the current series of simulations.

Since the three-dimensional dynamic equations of motion for the oblique fuze impact problem are intractable to solve in closed form, finite element methods are employed to obtain approximate solutions to the problem. A complete description of any boundary value problem in continuum mechanics involves specifying the geometry, boundary conditions, constitutive equations, and failure or instability criterion. The finite element solution for the unknown field variables (typically displacements) over the domain of interest proceeds by using the method of weighted residuals or through the development of a variational principle for the problem (see Zienkiewicz (1977) for a good review of finite element methods). As described in Zienkiewicz (1977), a global stiffness matrix is assembled at each time step to obtain a finite element solution. Alternatively, the equations of motion are directly integrated in EPIC92, thus circumventing the need for the formation of a stiffness matrix (Johnson 1977).

3.1 Geometry. A typical fuze geometry consists of a right-circular cone that threads into the projectile (Figure 1). The cutaway view also illustrates the important internal fuze components such as the firing pin, detonator, and booster. Although these complex components are necessary for operation

of the fuze under normal impact conditions, we replace them with a homogeneous material to simplify the analysis. Thus, the fuze model consists of an axially symmetric outerbody that encases an inner homogeneous core as shown in Figure 2. The base of the fuze is 2.40 in (61 mm) in diameter, and the fuze height is 3.72 in (94.5 mm) (Figure 2). The projectile consists of a solid right-circular cylinder, 1.0 in (25.4 mm) in diameter and 3.0 in (76.2 mm) long, and impacts the fuze normal to its axis of symmetry during EOD render-safe procedures.

3.2 Boundary Conditions. The boundary conditions are usually of mixed type and are given in terms of displacements, forces, or their first time-derivatives. The fuze is assumed to be rigidly fixed at the base so that all x-, y-, and z-displacements vanish on the base surface (Figure 2). We believe this assumption will not severely affect the results because the base of the actual fuze is tightly screwed into the ordnance (Figure 1). Since the core material is press-fit into the fuze outerbody, in the simulation we assume that the homogeneous brass core material is bonded to the fuze outerbody (Figure 2). The projectile impact velocity is 198 m/s, and numerical solutions are sought for two impact points along the vertical fuze axis (Figure 2). One impact point is 1.25 in (31.75 mm) below the top of the fuze, and the other impact point is 0.50 in (12.7 mm) above the base of the fuze; the bottom edge of the projectile impacts the fuze at these positions.

Finally, we assume that the contact surface between the projectile and the fuze is frictionless. It is difficult to estimate the severity of this assumption because of the lack of dynamic friction data for these materials. However, friction effects dominate the interactions of bodies in very low-speed or quasistatic contact problems. Thus, in the late stages of the impact event, as the projectile decelerates, friction will play a more important role in the interactions. A three-dimensional slide line algorithm permits the Lagrangian-based hydrocode to accommodate the severe distortions encountered in impact problems. This algorithm typically involves defining a master and slave surface, so as to prevent element interpenetration. A master surface and slave surface exist for both the projectile and the fuze in this analysis.

3.3 Constitutive Equations. The fuze outerbody material consists of 6061-T6 aluminum (EPIC92 material model 23) that encases an inner core of gun-cartridge brass (EPIC92 material model 2) (Figure 2). The projectile material consists of 4340 steel (EPIC92 material model 9). The initial simulation

results reveal that the projectile deforms more than that anticipated (Patel and Gold 1993). In subsequent analyses, we use a harder steel projectile, with a hardness of Rockwell C (Rc) Rc57. The properties of this material are based upon a modification of an Rc50, S-7 tool steel (EPIC92 material model 10) with a modified initial yield stress; the magnitude of the modified yield stress is based upon an empirical correlation that exists between Rockwell hardness and yield strength in various metals (see Oberg, Jones, and Horton 1984). The fuze deformation mechanisms observed for projectiles with these hardness values (Rc30 and Rc57) are very different, and therefore will be discussed and compared in more detail in Section 4.

The Johnson-Cook viscoplastic constitutive model is used in the analysis together with a von Mises initial yield condition (Johnson and Cook 1985; Johnson et al. 1992a,b). An isotropic hardening rule governs subsequent yield surface behavior. The equivalent uniaxial stress, $\bar{\sigma}$, is defined as

$$\bar{\sigma} = \sqrt{\frac{3}{2} \sigma_{ij}^{\prime} \sigma_{ij}^{\prime}} , \quad (1)$$

in which σ_{ij}^{\prime} is the deviatoric stress tensor. The Johnson-Cook model incorporates strain, strain rate, and thermal softening effects where the corresponding parameters functionally appear in multiplicative form as

$$\bar{\sigma} = \left[A + B \bar{\varepsilon}^{p^n} \right] \left[1 + C \ln \dot{\varepsilon}^* \right] \left[1 - T^*^m \right] , \quad (2)$$

in which $\bar{\varepsilon}^p$ is the equivalent time-dependent uniaxial plastic strain defined by

$$\bar{\varepsilon}^p(t) = \int_0^{\bar{\varepsilon}^p(t)} d\bar{\varepsilon}^p = \int_0^{\bar{\varepsilon}_{ij}^p(t)} \sqrt{\frac{2}{3} d\varepsilon_{ij}^p d\varepsilon_{ij}^p} , \quad (3)$$

and $d\varepsilon_{ij}^p = d\varepsilon_{ij} - D_{ijkl} d\sigma_{kl}$. D_{ijkl} is the fourth-rank elastic modulus tensor. $\dot{\varepsilon}^* = \dot{\varepsilon} / \dot{\varepsilon}_0$ is the dimensionless plastic strain rate for $\dot{\varepsilon}_0 = 1 \text{ s}^{-1}$, and T^* is the homologous temperature. The material constants A, B, C, n, and m are determinable from material tests conducted at different strains, strain rates, and temperatures

(Johnson et al. 1992a,b). The equivalent adiabatic flow stress versus equivalent plastic strain plots at strain rates of 1, 100 and 10,000 s⁻¹ are derived from the EPIC92 material library constants (Figure 3). All of the materials (except for brass) exhibit work-softening behavior which is a result of adiabatic thermal softening of dynamically strained material, rather than strength loss due to microcracking or other damage mechanisms.

3.4 Damage and Erosion Criteria. The damage criterion in EPIC92 is assumed to be a scalar function of the incremental (cumulative) equivalent plastic strain, $\Delta\bar{\epsilon}^p$, normalized with respect to the strain at fracture, ϵ^f (Johnson et al. 1992a,b):

$$D = \frac{\sum \Delta\bar{\epsilon}^p}{\epsilon^f} ; \quad (4)$$

where ϵ^f takes on a similar multiplicative form to that of Equation (2),

$$\epsilon^f = \left[D_1 + D_2 e^{D_3 \sigma^*} \right] \left[1 + D_4 \ln \dot{\epsilon}^* \right] \left[1 + D_5 T^* \right] , \quad (5)$$

in which $\sigma^* = \sigma_m / \bar{\sigma}$ is the pressure-stress ratio, σ_m is the pressure (mean stress), and D_1 through D_5 are independent material constants determined from fracture experiments. If $D \geq 1$ in Equation (4) in a given finite element, the element can only sustain additional hydrostatic compressive stress but not shear or tensile stresses. Unlike other finite element codes which can model the propagation of discrete fracture surfaces in the finite element mesh (Ingraffea 1989), EPIC92 cannot simulate such behavior. EPIC92 has the capability of handling the severe distortions encountered in penetration problems using an element erosion algorithm. The algorithm eliminates element volume, but retains element mass when a critical value of $\bar{\epsilon}^p$ is reached. In the current analysis, we consider that element volume erodes when $\bar{\epsilon}^p = 1.5$.

4. NUMERICAL RESULTS

The three-dimensional finite element mesh used to model the fuze consists of 544 symmetric brick finite elements; each brick element contains 24 tetrahedral elements that are formed by linking four

constant strain triangles (CSTs) (Figure 4). There are a total of 13,056 tetrahedral elements. The low-order displacement field within each CST element necessitates the use of more elements in regions of high-deformation gradient. One advantage of conducting the numerical analyses prior to the impact experiment is in determining the best time to radiograph the fuze. The results of the three-dimensional EPIC92 numerical simulations appear in Figures 5, 6, and 7. Figure 5 illustrates the "soft" projectile (Rc30) high-impact point results. Figures 6 and 7 illustrate the "hard" projectile (Rc57) high-impact and low-impact results, respectively.

4.1 Event 1. "Soft" Projectile, High-Impact Point. The "soft" projectile impacts the fuze ogive normal to the fuze axis of symmetry at a position located 1.25 in (31.75 mm) below the top (measured along the fuze axis) of the fuze. The projectile plastically deforms and rotates clockwise as it progressively slips towards the fuze apex (projectile rotation sense is relative to that shown in Figures 5, 6, and 7). The projectile's slipping motion scours a continuous groove of elliptical form into the fuze's surface. However, the groove is not so deep so as to expose the inner brass core of the composite fuze. After approximately 420 μ s of continuous contact, the projectile slips off the end of the fuze and continues rotating clockwise. After 1,200 μ s, the rear edge of the projectile rotates sufficiently to hit the fuze in a secondary impact event; this impact causes only minor additional fuze deformation. Because the projectile sustains large permanent deformations in our simulations, while Patel and Gold (1993) have observed that the projectile is relatively undeformed after impact, subsequent simulations use a harder steel projectile on the order of Rockwell C 57. The "hard" projectile material properties are essentially that of an S-7 tool steel (see Section 3.3, Constitutive Equations).

4.2 Event 2. "Hard" Projectile, High-Impact Point. Under identical impact conditions, and in contrast to the "soft" projectile impact, the "hard" projectile impact is relatively slip-inhibited and results in a greater penetration depth into the fuze than with the "soft" projectile. The "hard" projectile slips a negligible distance in the vertical direction, however, and rotates counterclockwise rather than clockwise, which can be seen by comparing Figures 5 and 6 at an elapsed time of 200 μ s. As in the "soft" impact event, the "hard" impact does not expose the brass core of the composite fuze. However, the "hard" projectile causes more deformation in the fuze than the "soft" projectile; a comparison of deformed meshes at 300 μ s in Figures 5 and 6 shows a greater degree of bending in the fuze impacted by the "hard" projectile. Hence, it appears that a "soft" projectile impact will cause less fuze damage

due to slip and permanent projectile deformation; the "hard" projectile causes more bending in the fuze and the projectile sustains less permanent deformation. The contact duration for the "hard" projectile impact is about 500 μ s, which exceeds the durations of the other two impact events.

Equivalent plastic strain, $\bar{\epsilon}^p$, contours aid in visualizing the permanent deformation history of the fuze (Figure 8). Equivalent plastic strain is a scalar representation of the tensorial strain state. The $\bar{\epsilon}^p = 0.20$ contours develop asymmetrically beneath the edge of the projectile after 20 μ s (Figure 8a). Plastic strain then spreads through the aluminum outerbody and reaches the brass core at 40 μ s. With increased projectile penetration and fuze bending, plastic deformation also appears on the back side of the fuze, and achieves $\bar{\epsilon}^p = 0.20$ at 120 μ s. The plastic zones eventually merge to form a plastic "hinge" through the cross section of the fuze. The projectile also deforms permanently, and $\bar{\epsilon}^p = 0.20$ is reached beneath the impact edge after 220 μ s. With continued bending of the fuze, the plastic hinge widens somewhat, but then remains steady throughout the remainder of the impact process.

4.3 Event 3. "Hard" Projectile, Low-Impact Point. In contrast to the "hard" high-impact event, the "hard" low impact causes much less fuze bending, primarily because the low impact occurs near the thick, rigidly fixed fuze base where the bending stiffness is large (Figure 7). Furthermore, because the impacted fuze surface is less oblique, the entire surface of the projectile contacts the fuze after 20 μ s. This reduces both projectile rotation and slip along the fuze surface. The equivalent plastic strain contours are nearly symmetric about the contact region (Figure 8b). In contrast to the high-impact event, the $\bar{\epsilon}^p = 0.20$ contours do not extend to the back side of the fuze, since there is not as much fuze bending. There is also a reduction in the contact time, and after 280 μ s the projectile bounces off the fuze in elastic rebound. The impact simulation results are summarized in Table 1.

Table 1. Summary of Impact Simulation Results.

shape of $\bar{\epsilon}^p = 0.20$ contours	projectile rotation rate ^a (rev/s) & sense	contact duration (μ s)	tip angle of neutral fiber ^a (deg)	tip displ. of neutral fiber ^a (mm)	projectile deformation
Event 1. "soft," high impact	w/s	232.8 CW	420	37.3	30.7
Event 2. "hard," high impact	asymmetric	-144.8 CCW	500	36.8	34.5
Event 3. "hard," low impact	symmetric	0.8 CW	280	3.7	7.9

^a at 700 μ s

5. IMPACT EXPERIMENTS

In the experiment a 300-g cylindrical steel projectile is launched at 208 m/s from a 37-mm gun with a barrel diameter of 1.090 in (27.7 mm). A schematic showing the relative positions of the fuze, projectile breakwire fixture for velocity measurement, x-ray tube and film plate, and 16-mm Hycam camera is given in Figure 9. The propelling charge consisted of 28 g of M2-165-mm gun propellant and was ignited using an M38 B-2 primer. An obturator was attached to the projectile during firing to reduce combustion gas emissions. Several pretest shots verified the projectile velocity repeatability. The aim point was 1.25 in (31.75 mm) below the fuze top, but the actual impact point was 0.27 in (6.8 mm) below the aim point. Based on the results of the simulation, it was desired to have a radiographic image of the impact event taken 250 μ s after initial impact. The actual radiograph was taken 272 μ s after impact, and we compared this radiograph with the hydrocode results at 280 μ s (Figure 10). At this instant, the brass core of the fuze is bent but not fractured, and the aluminum outerbody appears fractured through the cross section. The projectile deforms by slightly bulging beneath the point of impact, and the projectile's tail end is rotated slightly upward at this instant in the impact.

The steel projectile penetrated into the fuze to a maximum depth of approximately 13 mm and formed a circular indentation in the aluminum. The aluminum subsequently fractured, and the fuze top was severed (Figure 11). The fuze top fragment also contained a circular impact imprint in its surface. Also visible in Figure 11 is the bolt that holds the fuze to the 0.25-in (6.35 mm)-thick rolled-homogeneous armor (RHA) base and the failed weld line in the RHA base plate. The weld in the RHA base plate failed during impact, and the entire fuze assembly rotated backwards approximately 35 degrees. This was an unanticipated fixture failure, and prevented quantitative comparisons between the experimental and numerical fuze deformation results. The projectile sustained little permanent deformation, although a small chip was visible on the edge beneath the impact point.

6. COMPARISON OF NUMERICAL AND EXPERIMENTAL RESULTS

The experimental results and the simulation results generally agree during the initial stages of the impact but depart significantly at later stages of the penetration. The reasons for the observed differences between the simulation and the experiment appear in the discussion following, and are related to: 1) the

inability of the hydrocode to effectively model fracture, and 2) boundary condition differences between the experiment and those assumed in the numerical simulation.

The most obvious difference between the experimental results and our predictions is that in the experiment, the fuze failed by fracture, while we predicted that the top of the fuze remained intact and connected to the fuze body for identical impact conditions. Despite the fact that the plastic "hinge" might suggest a failure location, the inability of the hydrocode to model gross, large-scale fracture in structures is a primary reason why there is a disparity between numerical impact results and the experiment. Instead, the hydrocode simulates fracture failure by eliminating an element's ability to sustain shear and tensile normal stress when the level of damage exceeds a critical level in that element. To address this type of fracture problem, the EPIC92 hydrocode would require an algorithm that permits finite element mesh bifurcation when a critical energy release rate is attained or by using specialized crack-tip singularity finite elements (Ingraffea 1989).

The boundary conditions are somewhat different between the experiment and the numerical simulation, despite our efforts to minimize them. Boundary condition differences include: 1) modeling the contact surface as a frictionless interface, whereas in reality, contact friction can influence the deformation in low-speed impact problems, 2) a disparity in the impact point and impact velocity between the experiment and the simulation (additional hydrocode simulations could have been conducted to match the actual impact point in the experiment; however, the additional time and expense needed to conduct the additional simulations would not have added further insight into the render-safe problem, since the fundamental fracture physics could not be modeled by the hydrocode), and 3) interface bonding differences between the brass core and the aluminum outerbody. Recall that in the experiment, the brass core was press-fit into the aluminum outerbody and that given enough force, slip could occur along this interface. The interface was modeled so as to prevent slip in the numerical simulation. Furthermore, failure of the weld line in the experiment permitted the fuze body to rotate at its base, whereas the base of the fuze was rigidly fixed in the numerical simulation.

7. ANALYTICAL APPROACH

The fuze-projectile problem addressed earlier is reminiscent of a cantilever beam that is subjected to transverse impact. Although a complete review of the vast literature available on this topic is beyond the scope of this report, some notable works relevant to the current problem should be mentioned. Much of the original research on the transverse impact of elastic-plastic beams was funded by organizations such as the Office of Naval Research and can be found, for example, in early issues of publications such as the ASME Journal of Applied Mechanics. Both Lee and Symonds (1952) and Parkes (1955) investigated the extent of applicability of using the methods of static plasticity solutions to dynamic problems. Their rigid-plastic analyses predict the development of a moving plastic "hinge." Interestingly, a plastic hinge develops beneath the projectile in Event 2 (Figure 8), a deformation feature which is common in problems addressed in the literature involving both quasistatic and impulsively loaded elastic-plastic beams. For short beams, the effect of shear deformations are no longer negligible and their effects can be estimated by construction of so-called *interaction curves*, using a plane stress approach (Green 1954; Drucker 1956) or using a variational approach (Hodge 1957). Hodge's (1957) analysis shows that for simply supported elastic-plastic short beams in which beam thickness is approximately equal to beam length (as in this work), the maximum load that the beam can sustain is reduced by approximately 20% if one includes the effects of shear in the analysis. Some of the discrepancies between theory and experiment discussed in Parkes' (1955) paper were reexamined by Ting (1964, 1965), whose analyses rigorously account for geometrical effects due to large plastic deformations of the rigid-plastic beam. Keer and Schonberg (1986) solve an elastic cantilever beam problem subjected to two types of indentation displacement fields using a local elasticity solution coupled to a global beam theory solution approach. Both the local deformation effects of the indentor as well as the global deformation of the cantilever beam are modeled; however, the solution is limited to elastic media. Finally, Shu et al. (1992) describe the mechanics of oblique impact of impulsively loaded cantilever beams in terms of axial and flexural components. Their model includes a mass of *finite* size at the beam tip, which produces a double "hinge" deformation mechanism. The model is used to explain why the observed curvature of the beam tip is less than that predicted by Parkes' (1955) single- "hinge" model. Closed-form three-dimensional analytical solutions for transient loading of composite elastic-plastic bodies of variable cross section do not appear in the literature, so a precise comparison with the hydrocode results is not possible. A closed-form solution to the elastic-plastic short beam impact problem would be invaluable to the explosive ordnance disposal community.

Often, the analytical solution to the "real" structural mechanics problem is intractable, whereas useful solutions can be obtained for a reduced or simplified version of the original problem. In this spirit, we consider the problem of an elastic perfectly-plastic cantilever beam of circular cross section subjected to transverse impact as a model of the fuze impact problem. The analysis uses elementary beam theory with the following additional simplifying assumptions:

- 1) There is small deformation theory.
- 2) There is negligible beam inertia.
- 3) The beam material is homogeneous (not composite) and elastic perfectly-plastic.
- 4) There are negligible shear stresses.

The remainder of this section is devoted to developing a simple analytical cantilever beam model of the fuze for estimating the total amount of strain energy absorbed by the fuze during impact. The analytical model results are then compared with the hydrocode predictions.

7.1 Deflections of a Cantilever Beam. The deflection curve of a beam can be shown to be governed by the following second-order ordinary differential equation (Timoshenko and Gere 1972),

$$\frac{d^2v}{dx^2} = -\frac{M}{EI} = \kappa \quad , \quad (6)$$

in which v is the deflection, M is the bending moment applied to the beam, E is Young's modulus, I is the cross-sectional moment of inertia about the neutral axis, and κ is the curvature of the neutral axis. The quantity EI is known as the flexural rigidity of the beam. Two successive integrations of Equation (6), with boundary conditions, $v(L) = v'(L) = 0$ (Figure 12a), provide the solution, $v(x)$, for an end-loaded cantilever beam as

$$v(x) = \frac{Px^3}{6EI} - \frac{PxL^2}{2EI} + \frac{PL^3}{3EI} \quad , \quad (7)$$

in which L is the beam length, P is the magnitude of the end load, and the bending moment is given by $M = -Px$. The maximum deflection occurs at the cantilever tip, $x = 0$, and is given by

$$v_{\max} = \frac{P L^3}{3 E I} \quad . \quad (8)$$

7.2 Elastic-Plastic Deflections of a Cantilever Beam. Moment equilibrium of stress about the neutral axis of the beam yields the following integral expression for the resultant bending moment as

$$M = \iint_A \sigma y dA \quad , \quad (9)$$

in which σ is the longitudinal stress acting normal to an element of cross-sectional area, dA , and y is the distance from the neutral axis to dA . The fundamental assumption in slender beam theory is that plane sections remain plane and normal to the longitudinal fibers of the beam so that the longitudinal strain $\epsilon = \kappa y$. For a beam made of an elastic (Hookean) material we have, $\sigma = E \epsilon$, thus,

$$\sigma = \kappa E y \quad . \quad (10)$$

It is clear from Equation (10) that the maximum stress occurs at the outer fibers of the beam (Figure 12b). For an elastic perfectly-plastic material the maximum stress is the yield stress (Figure 12c), and we have

$$\sigma_y = \kappa E e \quad , \quad (11)$$

in which e is the distance from the neutral axis to the edge of the elastic core (Figure 12b). Substitution of Equation (10) and Equation (11) into Equation (9) and using $(dA) = 2z(dy)$ in Equation (9) for a beam of circular cross section and diameter h , we arrive at

$$M = \int_{-h/2}^{h/2} \sigma y dA = \frac{2\sigma_y}{e} \int_{-e}^e y^2 \sqrt{\left(\frac{h}{2}\right)^2 - y^2} dy + 4\sigma_y \int_e^{h/2} y \sqrt{\left(\frac{h}{2}\right)^2 - y^2} dy \quad , \quad (12)$$

or,

$$M = \frac{3\sigma_y \sin^{-1}(2e) h^4 + \sqrt{h^2 - 4e^2} (10eh^2 - 16e^3) \sigma_y}{96e} \quad . \quad (13)$$

The first integral on the right-hand side of Equation (12) represents the contribution to the bending moment due to elastic stresses, while the second integral in Equation (12) represents the contribution to the bending moment due to plastic flow. Yielding begins to occur in the circular beam when $M = M_y$, or when

$$\lim_{\epsilon \rightarrow h/2^+} M = M_y , \quad (14)$$

which gives for the *yield moment*, M_y , for the circular beam,

$$M_y = \frac{\sigma_y h^3 \pi}{32} . \quad (15)$$

As the bending moment of the beam increases, the region of purely elastic behavior shrinks until the maximum or limiting moment in the beam is reached. The limit is known as the *plastic moment*, M_p , and is obtained as

$$\lim_{\epsilon \rightarrow 0^+} M = M_p . \quad (16)$$

For the beam of circular cross section the plastic moment is given by

$$M_p = \frac{\sigma_y h^3}{6} . \quad (17)$$

Timoshenko and Gere (1972) define a *shape factor*, f , for a beam of given cross-sectional geometry as the ratio of the plastic moment to the yield moment, or $f = M_p/M_y$. For a beam of circular cross section, $f = 16/3\pi \approx 1.70$, as obtained by dividing Equation (17) by Equation (15). In the linear-elastic range, the relation between bending moment and curvature can be nondimensionalized (Timoshenko and Gere 1972) as follows,

$$\frac{M}{M_y} = \frac{\kappa}{\kappa_y} , \quad 0 \leq M \leq M_y . \quad (18)$$

Equation (18) is a linear function on a moment-curvature diagram (Figure 13). However, as M increases beyond M_y , and the beam begins to yield, the moment-curvature relationship becomes nonlinear and the ordinate value approaches an asymptote representing the plastic moment, M_p , which is equivalent to the shape factor, f , as shown in Figure 13. In the nonlinear range, the bending moment in Equation (13) is nondimensionalized by dividing by Equation (15) to obtain

$$\frac{M}{M_y} = \frac{3 \sin^{-1} \left(\frac{2\kappa_y}{\kappa} \right) \left(\frac{\kappa}{\kappa_y} \right)^4 + \sqrt{\left(\frac{\kappa}{\kappa_y} \right)^2 - 4} (10 \left(\frac{\kappa}{\kappa_y} \right)^2 - 16)}{3\pi \left(\frac{\kappa}{\kappa_y} \right)^3}, \quad (19)$$

in which $\kappa/\kappa_y = h/2e$. By way of comparison, it can be shown that the moment-curvature relation for a rectangular beam takes on the relatively simple form (Timoshenko and Gere 1972),

$$\frac{M}{M_y} = \frac{3}{2} \cdot \frac{\kappa_y^2}{2\kappa^2}, \quad M_y \leq M \leq M_p, \quad (20)$$

which can be solved for the curvature ratio in terms of the moment ratio as follows,

$$\frac{\kappa}{\kappa_y} = \frac{\sqrt{2}/2}{\sqrt{\frac{3}{2} - \frac{M}{M_y}}} , \quad M_y \leq M \leq M_p . \quad (21)$$

The presence of the arcsine function in Equation (19) makes the direct algebraic solution for κ/κ_y difficult. However, an approximate solution may be obtained by plotting Equation (19) for given values of κ/κ_y and curve fitting the resulting nonlinear equation using a Marquardt-Levenberg (M-L) regression algorithm (Press et al. 1986). Equation (19) is plotted (Figure 14) together with the following approximation obtained using the M-L method,

$$\frac{\kappa}{\kappa_y} \approx \frac{\sqrt{3}/2}{\sqrt{\frac{16}{3\pi} - \frac{M}{M_y}}} , \quad M_y \leq M \leq M_p , \quad (22)$$

where we have replaced the M-L derived numerical value, 0.86810, in the numerator of Equation (22), with $\sqrt{3}/2$ to more closely resemble the form of the numerator in Equation (21). Before we can determine the strain energy in the beam, we must determine the tip deflection, δ , as a function of the applied load, P . The tip deflection, δ , of the elastic-plastic beam may be determined by use of the *second curvature-*

area theorem (Timoshenko and Gere 1972, pp. 306-309) as follows,

$$\delta = \int_0^{x_1} \frac{P x^2}{EI} dx + \int_{x_1}^L \kappa x dx , \quad (23)$$

in which x_1 represents the limit of purely elastic behavior in the beam. The tip deflection is evaluated by first substituting the approximate curvature expression (Equation 22) into the integrand of the second integral in Equation (23), and using the identities, $\kappa_y = M_y/EI$, $x_1 = M_y/P$, and $M_y = P_y L$. This results in the following approximate expression for the dimensionless deflection (plotted in Figure 15),

$$\frac{\delta}{\delta_y} = \left(\frac{P_y}{P} \right)^2 \left[7.37 - 5.89 \left(1 + 0.294 \frac{P}{P_y} \right) \sqrt{\frac{16}{3\pi} - \frac{P}{P_y}} \right] , \quad 1 \leq \frac{P}{P_y} \leq \frac{16}{3\pi} , \quad (24)$$

in which $\delta_y = \frac{P_y L^3}{3EI}$ (from Equation (8)) is the maximum elastic deflection at the yield load P_y . When

$\frac{P}{P_y} = \frac{16}{3\pi}$, the dimensionless deflection is $\frac{\delta}{\delta_y} = 2.55$.

7.3 Complementary Energy of an Elastic-Plastic Cantilever Beam. The dimensionless complementary energy, U^* , in a beam subjected to inelastic bending may be obtained by integrating Equation (24) with respect to P/P_y as

$$U^* = \int_0^1 \frac{P}{P_y} d\left(\frac{P}{P_y}\right) + \int_1^{P_1} \frac{\delta(P/P_y)}{\delta_y} d\left(\frac{P}{P_y}\right) . \quad (25)$$

The first term in Equation (25) is the elastic contribution to the complementary energy, while the second term is the elastic-plastic contribution to the complementary energy. Evaluation of these integrals gives the total dimensionless complementary energy of the beam,

$$U^* = \frac{1}{2} + \left(2\sqrt{3}(f-p_1)\sqrt{f-p_1} + (p_1-1) + \sqrt{3}\sqrt{f-1} (3p_1 - 2f - 1) \right) / p_1 , \quad (26)$$

in which $P_y = \frac{P}{P_y}$ and $f = \frac{16}{3\pi}$. At the maximum bending load, $P_y = f = \frac{16}{3\pi}$, and $U^* = \frac{1}{2} + 1.005 = 1.505$ in

Equation (26). Also,

$$U^* + U = \frac{P}{P_y} \frac{\delta}{\delta_y} , \quad (27)$$

in which U is the dimensionless strain energy of the beam. Hence in Equation (27), $U = (16/3\pi)(2.55) - 1.505 = 2.82$. This result shows that the total dimensionless strain energy, at the moment the plastic hinge is formed, is over 4.5 times the energy absorbed in the purely elastic bending regime. The ratio of plastic bending strain energy to total elastic bending strain energy is thus $(2.82 - 8/3\pi)/(8/3\pi) = 2.32$.

8. COMPARISON OF NUMERICAL AND ANALYTICAL RESULTS

In order to determine the strain energy in the elastic-plastic beam, we must first calculate realistic values of P_y and δ_y using the material properties of 6061-T6 aluminum. To simplify the analysis, the effect of the brass core material on the inelastic bending of the cantilever beam is not considered. We assume in our analysis that the cantilever beam is composed entirely of aluminum which is "stronger" than the brass up to an equivalent plastic strain of 0.20 (Figure 3). Therefore, for a given deflection, our analysis would overestimate the beam bending strain energy for $\bar{\epsilon}^p \leq 0.20$, and underestimate the strain energy for $\bar{\epsilon}^p > 0.20$. However, a composite beam solution could be obtained by generalizing Equation (12) to account for contributions to the moment equilibrium from both the brass and aluminum materials. The load at the onset of yield is a strong function of beam thickness, h , and is given by

$$P_y = \frac{M_y}{L} = \frac{\sigma_y h^3 \pi}{32 L} , \quad (28)$$

and the deflection at yield is

$$\delta_y = \frac{\sigma_y h^3 \pi L^2}{96 EI} = \frac{2\sigma_y L^2}{3 E h} , \quad (29)$$

in which the moment of inertia $I = \frac{\pi h^4}{64}$. With $\sigma_y = 3.25$ kbars (4.7×10^4 psi), $L = 2.47$ in (62.7 mm) (measured from the impact point to the base), $E = 739$ kbar (1.07×10^7 psi), $h = 2.4$ in (61 mm), Equations (28) and (29) give, $P_y = 25,893$ lbf (115 kN), and $\delta_y = 0.0074$ in (0.188 mm).

The effect of beam taper can be analyzed by recognizing that the fuze geometry consists of a nonprismatic (tapered) cone in which the diameter can be approximated with the expression $h = h(x) = h_a + (h_b - h_a)x/L$. It can be easily shown by substitution of $h(x)$ into Equation (28) that the load, P_y , required to cause yield, is a function of position along the length of the cone of diameter, h_a , at the impact location, and of diameter, h_b , at the built-in end. Therefore Equation (28) can be rewritten as

$$P_y = \frac{\sigma_y \left(h_a + (h_b - h_a) \frac{x}{L} \right)^3 \pi}{32 x} , \quad (30)$$

with similar substitutions required in the expressions for beam inertia, I , and deflection, δ_y . In a prismatic cantilever beam, the positions of maximum stress, σ_{max} , and bending moment are coincident and occur at the built-in end with diameter, h_b . However, in a tapered cantilever beam, we find that the maximum stress is

$$\sigma_{max} = \frac{128 P L}{27 \pi h_a^2 (h_b - h_a)} , \quad \text{at } x = \frac{h_a L}{2(h_b - h_a)} , \quad (31)$$

in which the position of σ_{max} is determined by setting $d\sigma_y/dx = 0$ in Equation (30). In the fuze problem, $h_b = 2.4$ in (61 mm) and $h_a = 1.39$ in (35.3 mm), so that σ_{max} occurs at $x = 0.689L$, measured from the impact point toward the built-in end. In addition, we find that the ratio of maximum stress, σ_{max} , to the stress, σ_b , in the built-in end of the tapered beam to be

$$\frac{\sigma_{max}}{\sigma_b} = \frac{4h_b^3}{27 h_a^2 (h_b - h_a)} , \quad (32)$$

in which, for the specific case of the fuze geometry, we find that σ_{max} is 5% greater at $x = 0.689L$ than σ_b at $x = L$ (σ_b is determined by letting $x=L$ in Equation (30)). For the specific case of a tapered circular cantilever beam in which $h_b = 2 h_a$, Timoshenko and Gere (1972) find a 19% increase in σ_{max} relative to σ_b which occurs at $x = 0.5L$. Our result in Equation (32) is more general, however, and reduces to the Timoshenko and Gere (1972) result when $h_b = 2 h_a$. The assumption that the fuze geometry is prismatic is not so bad since there is only a 5% difference between σ_{max} and σ_b in a beam with the fuze geometry considered in this work.

An estimate of the average load, P , on the cantilever beam can be determined from the length of time it takes the projectile to decelerate and begin to rebound. Inspection of the fuze centerline nodal position versus time plot (Figure 16) indicates that the projectile's velocity reversed at about 360 μs and that the amount of elastic rebound beneath the projectile is about 0.0298 in (0.747 mm). The change in the projectile's momentum with respect to time is equal to the average impact force $P = 37,094$ lbf (165 kN), which is determined using an initial projectile velocity of 198 m/s and mass of 0.3 kg. The beam theory solution provided the value of $P_y = 25,893$ lbf (115 kN) from Equation (28), so that $P/P_y = 1.43$. Since P_y is sensitive to the value chosen for h (see Equation (28)), if a slightly smaller value of h were used in the calculation (rather than the maximum value used of $h_b = h = 2.4$ (61 mm)), P_y would dramatically decrease, and P/P_y would become $f = M_p/M_y = 16/3\pi = 1.7$. At this limit the beam is in a state of unrestricted plastic flow. A state of unrestricted plastic flow occurs in the fuze very early in the deformation history, as seen in the well-developed pattern of plastic strain through the fuze cross section at 120 μs (Figure 17). The total strain energy absorbed by the fuze during impact can be estimated by assuming that $P/P_y = M_p/M_y = 16/3\pi = 1.7$ and $\delta_y = 0.0074$ in (0.188 mm) from Equation (29). The actual deflection beneath the load point from the numerical simulation at 360 μs is $\delta = 0.657$ in (16.7 mm), which results in $\delta/\delta_y = 89$. Hence, the total dimensionless strain energy absorbed by the fuze due to elastic-plastic bending is estimated with the aid of Figure 15 to be

$$U_{Tot} = \frac{P}{P_y} \frac{\delta}{\delta_y} - 2.55 + U = \frac{16}{3\pi} (89 - 2.55) + 2.8 = 149.5 \quad . \quad (33)$$

This energy is dimensionalized through multiplication by $P_y \delta_y$, which results in a total strain energy of 2,387 ft-lbf or 3.24 kJ, attributed to elastic-plastic bending of the fuze. The 0.3-kg projectile can impart 5.88 kJ of kinetic energy during impact. Therefore, the plastic bending energy is 55% of the initial

projectile kinetic energy. The fuze also suffered a considerable amount of localized deformation beneath the projectile (Figure 17). The energy absorbed by this localized deformation can be approximated by multiplying the average projectile indentation depth, δ_p (estimated from the experiment), with the average impact force, P , resulting in $P\delta_p = (37,094)(0.45)$ in lbf = 1.89 kJ. This localized plastic energy is 32% of the initial projectile kinetic energy. Hence, the energy absorbed in fuze bending is about 1.7 times greater than the energy dissipated by localized deformation beneath the projectile. In the Event 2 simulation, the EPIC92 code estimates that the total plastic work absorbed by the fuze is 91% of the initial projectile kinetic energy, which is in close agreement to our analysis, which predicts that 87% of the initial projectile kinetic energy is dissipated in plastic work. The EPIC92 code also predicts that the rotational kinetic energy associated with the rebounding projectile is only 1% of the initial projectile kinetic energy.

The analytical model of an elastic-plastic beam subjected to an end load provides insight, at least to the point of fracture, into the render-safe mechanics of fuzes. It is estimated that 55% of the initial projectile kinetic energy is dissipated in elastic-plastic fuze bending and 32% of the energy is dissipated in localized deformation beneath the projectile. These results are corroborated by the EPIC92 numerical results, which predict that 91% of the projectile kinetic energy is dissipated into target plastic work; the remaining energy is primarily dissipated as plastic work in deforming the projectile.

9. CONCLUSIONS

- 1) The results of numerical hydrocode simulations of oblique impact of a cylindrical steel projectile onto an aluminum-brass composite fuze simulant indicate that projectile hardness is an important parameter that governs the deformation history of the fuze; a "soft" steel projectile impacted the fuze and created a gouge, elliptical in form, as it ricocheted off the fuze, whereas a "hard" steel projectile penetrated to a greater depth and bounced obliquely off the fuze.
- 2) Reasons for the observed disparity between the experiment and the hydrocode simulation of a materially and geometrically identical fuze impact problem include: 1) the inability of the hydrocode to effectively model global fracture, and 2) boundary condition differences between the experiment and the numerical simulation; in the experiment a weld line failed, which provided an additional rotational

degree of freedom, whereas in the numerical simulation the fuze maintained a rigid base. Nonetheless, the plastic "hinge" predicted in the simulation might suggest an indication of where the failure might be expected to occur.

3) The projectile's sense of rotation during impact is related to projectile hardness and impact point as the numerical simulations indicate that the projectile 1) rotates clockwise in impact Event 1, involving the "soft" projectile, because of slip between the projectile and fuze, 2) rotates counterclockwise in impact Event 2, involving the "hard" projectile, since the harder projectile penetrates into the fuze, thereby precluding slip, and 3) remains relatively level in impact Event 3 as the obliquity of impact is less than in Events 1 and 2.

4) Positioning the gun close to the fuze during firing provides a lateral constraint to the projectile during impact. This practice would help prevent projectile rotation during flight and impact and would also reduce the variability in impact response that occurs as a result of projectile impact obliquity, impact location, and projectile hardness effects.

5) An analytical model of a cantilevered elastic-plastic beam subjected to an end load provides insight, at least to the point of fracture, into the render-safe mechanics of fuzes. For the case studied, it is estimated that 55% of the initial projectile kinetic energy is dissipated in elastic-plastic fuze bending and 32% of the energy is dissipated in localized deformation beneath the projectile. These results are corroborated by the EPIC92 numerical results, which predict that 91% of the projectile kinetic energy is dissipated into target plastic work; the remaining energy is primarily dissipated as plastic work in deforming the projectile.

INTENTIONALLY LEFT BLANK.

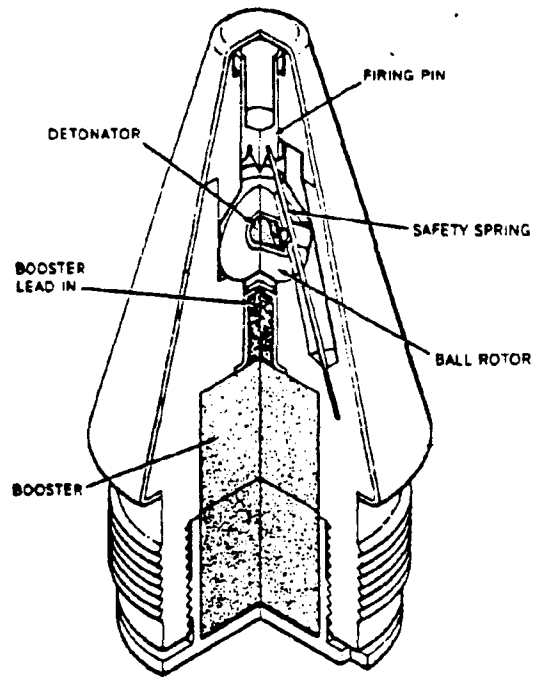


Figure 1. Cutaway View of a Typical Fuze, Illustrating Internal Components.

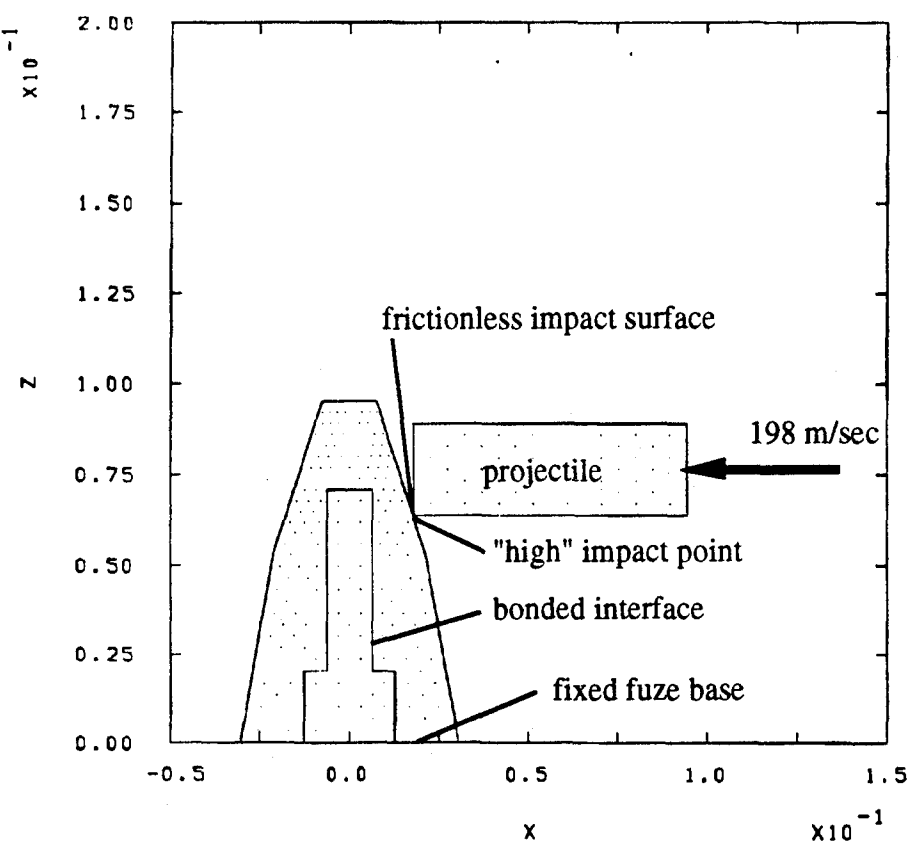


Figure 2. Fuze and Projectile Boundary Conditions (dimensions in meters).

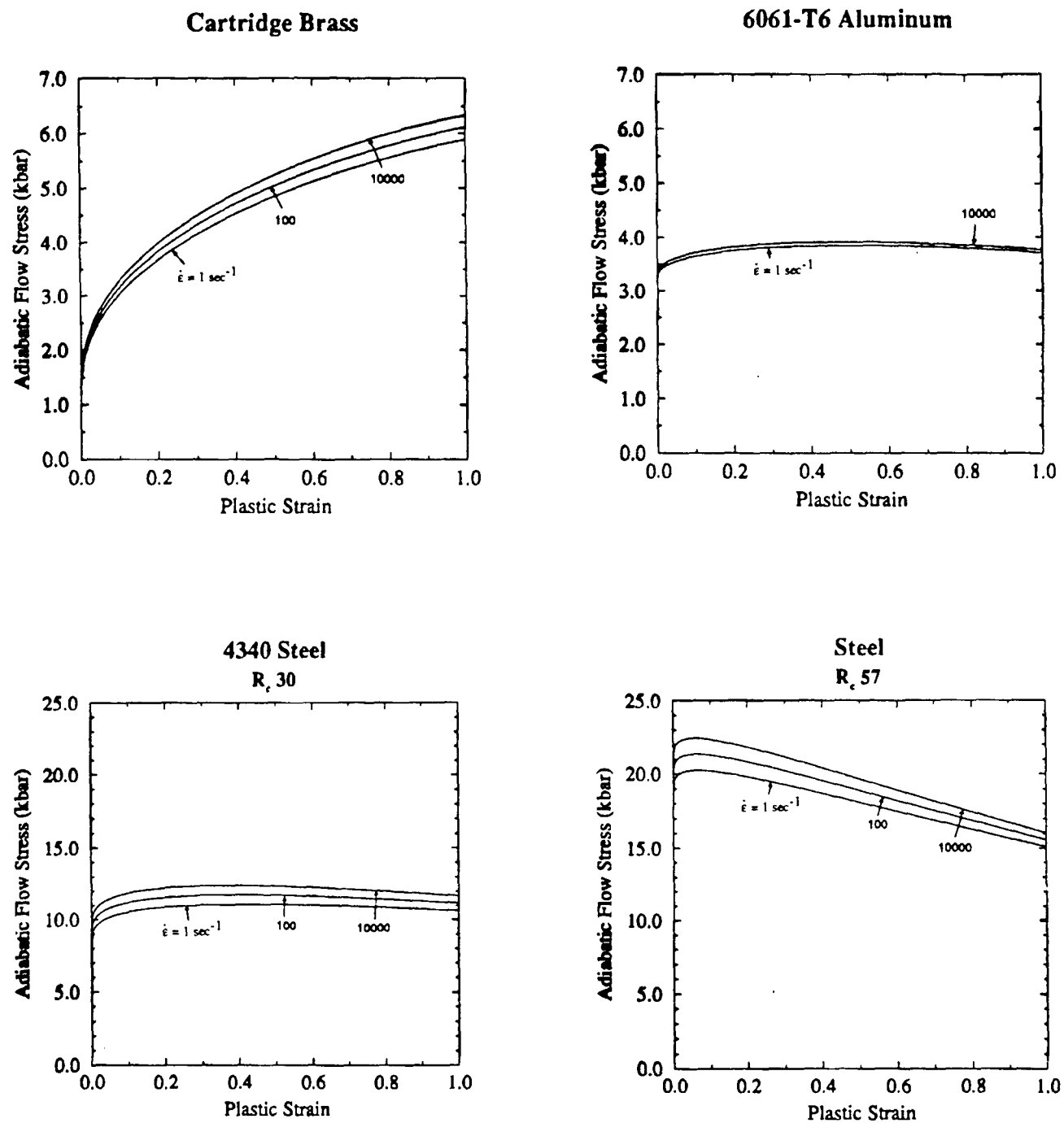


Figure 3. Adiabatic Flow Stress Versus Equivalent Plastic Strain Curves as a Function of Strain Rate for Gun Cartridge Brass, 6061-T6 Aluminum and 4340 and Modified S-7 Tool Steels.

- 514 symmetric brick finite elements
- 24 tetrahedral elements per brick
- 13,056 total tetrahedral elements
- 4 constant strain triangles per tetrahedron
- 52,224 CST's

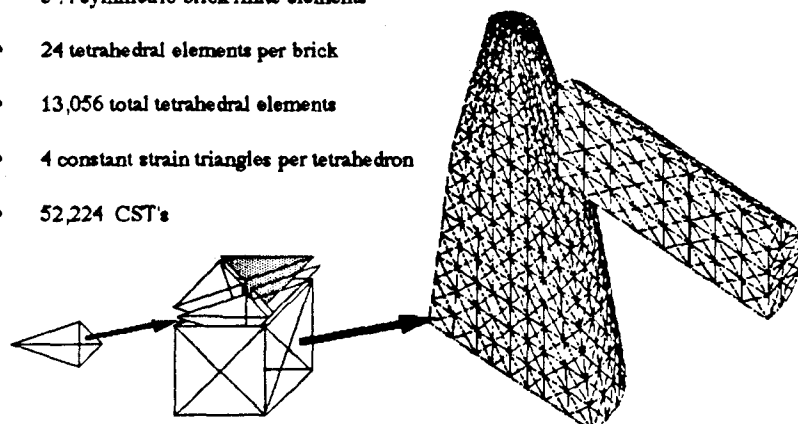


Figure 4. Finite Element Mesh Used in Numerical Simulations.

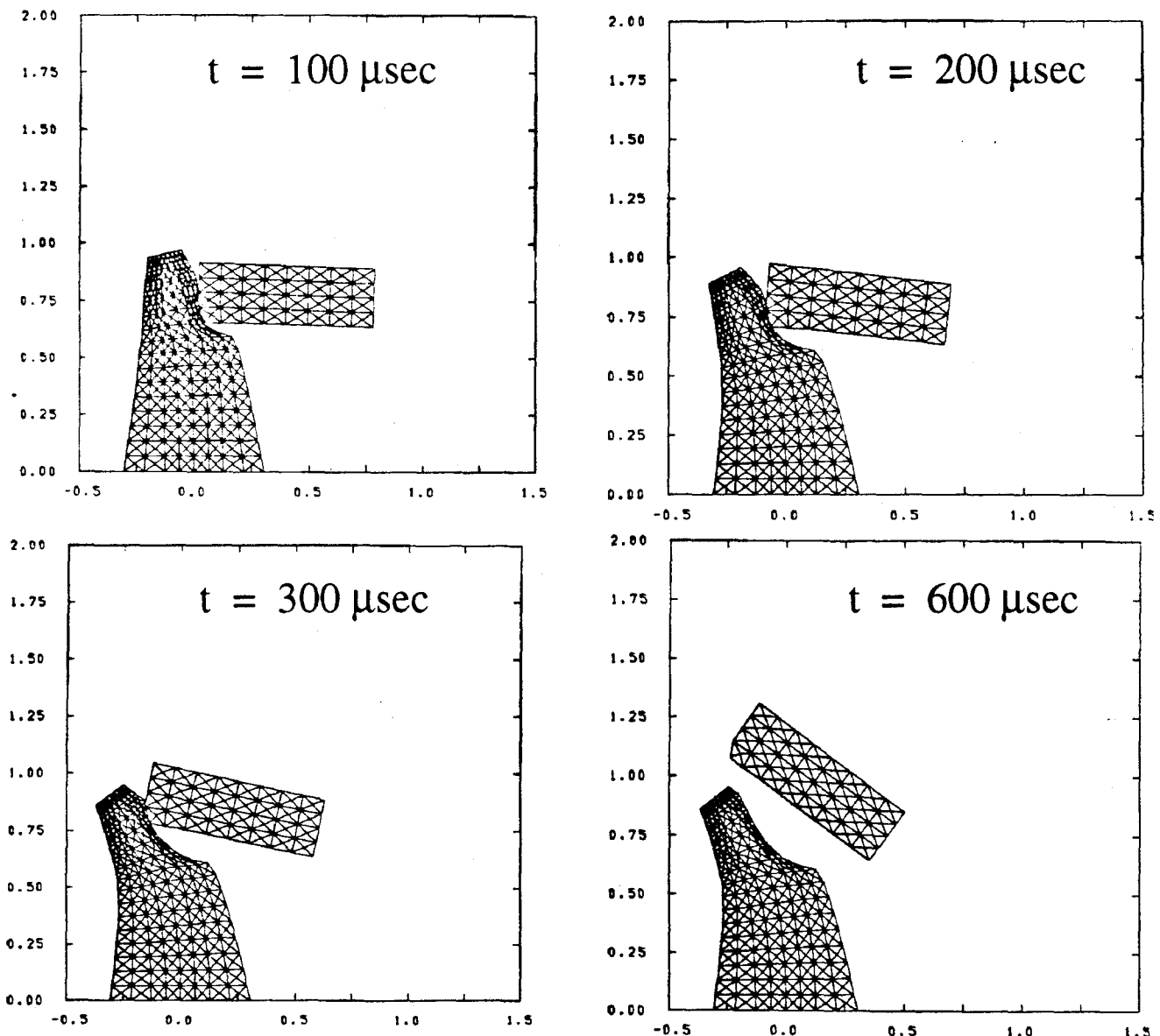


Figure 5. Event 1. "Soft" High-Impact EPIC92 Hydrocode Results.

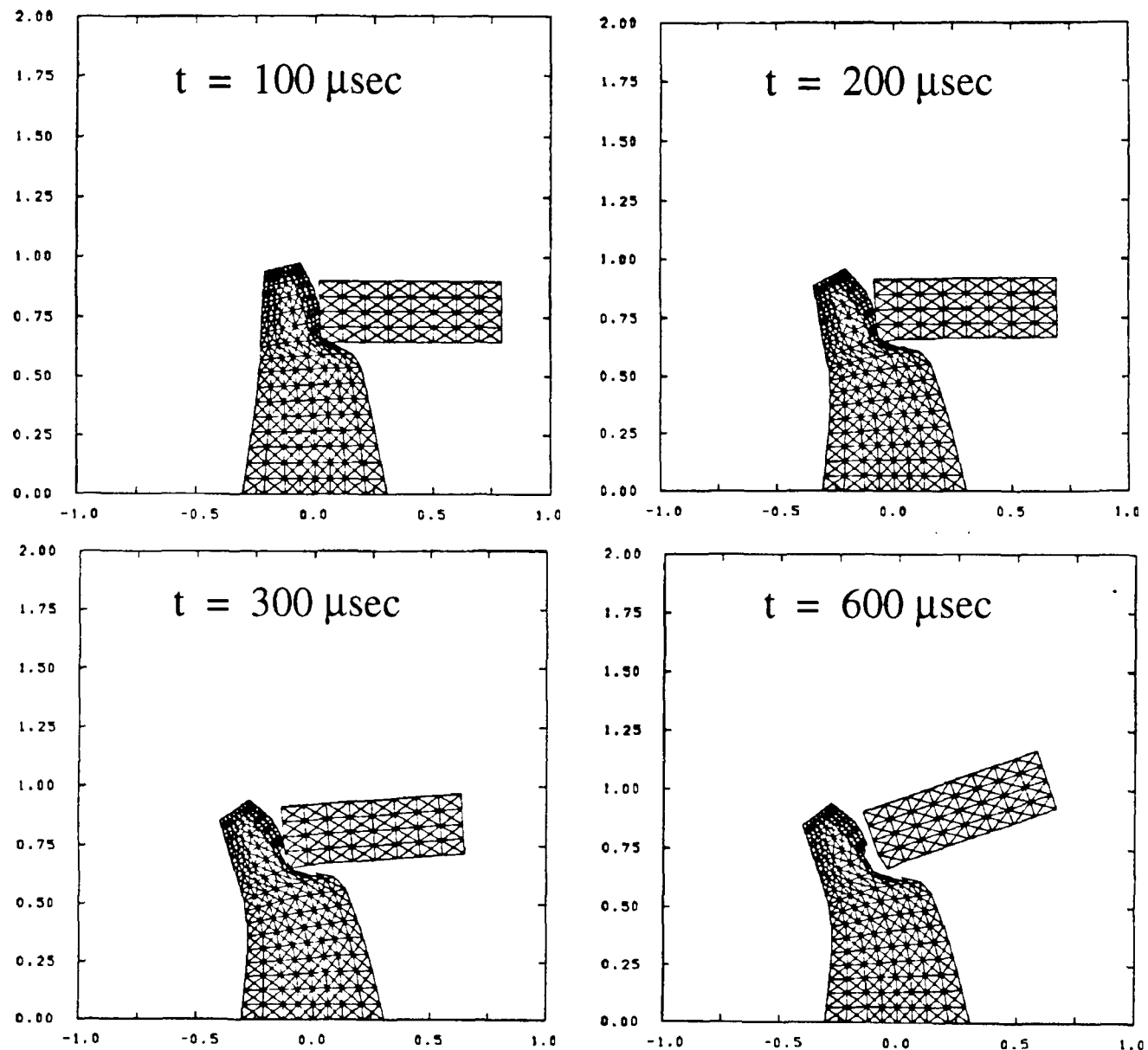


Figure 6. Event 2, "Hard" High-Impact EPIC92 Hydrocode Results.

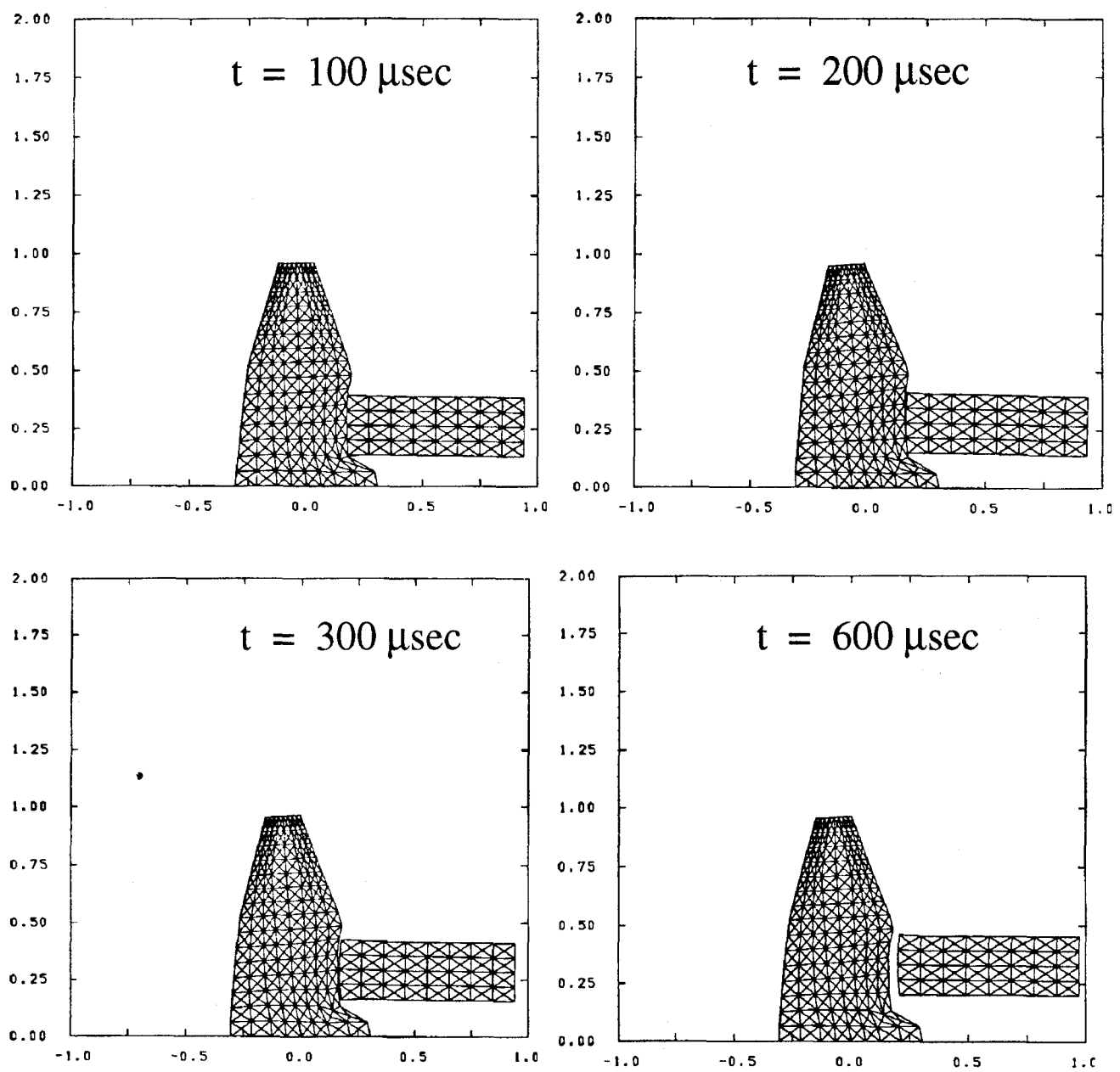
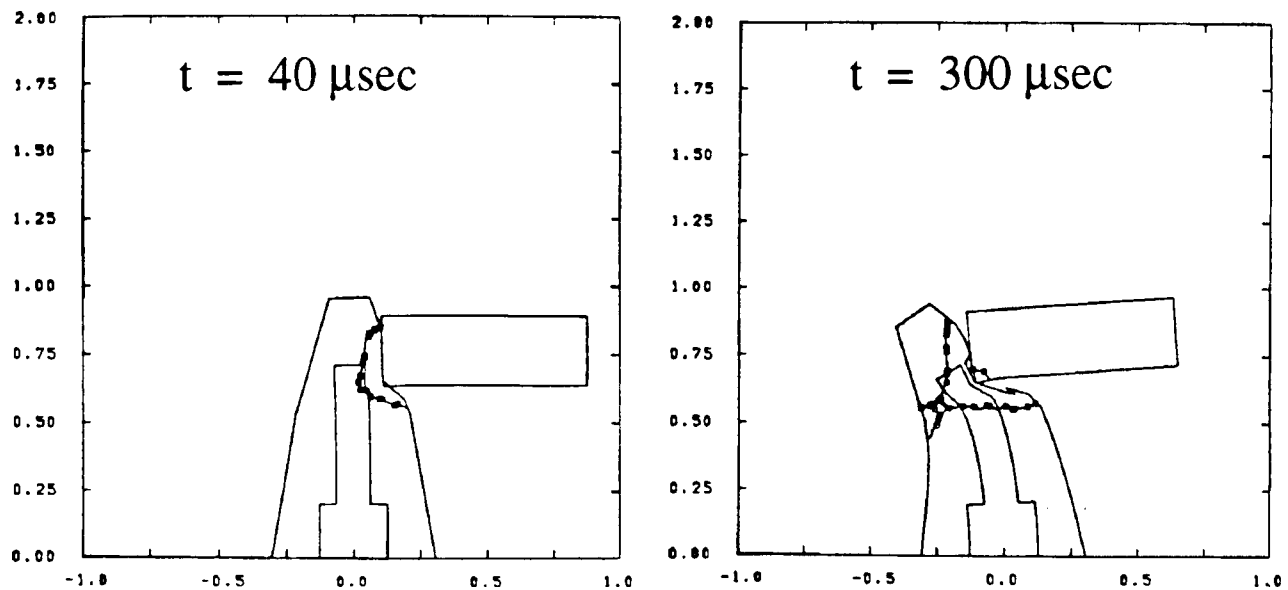


Figure 7. Event 3. "Hard" Low-Impact EPIC92 Hydrocode Results.

a) Event 2.



b) Event 3.

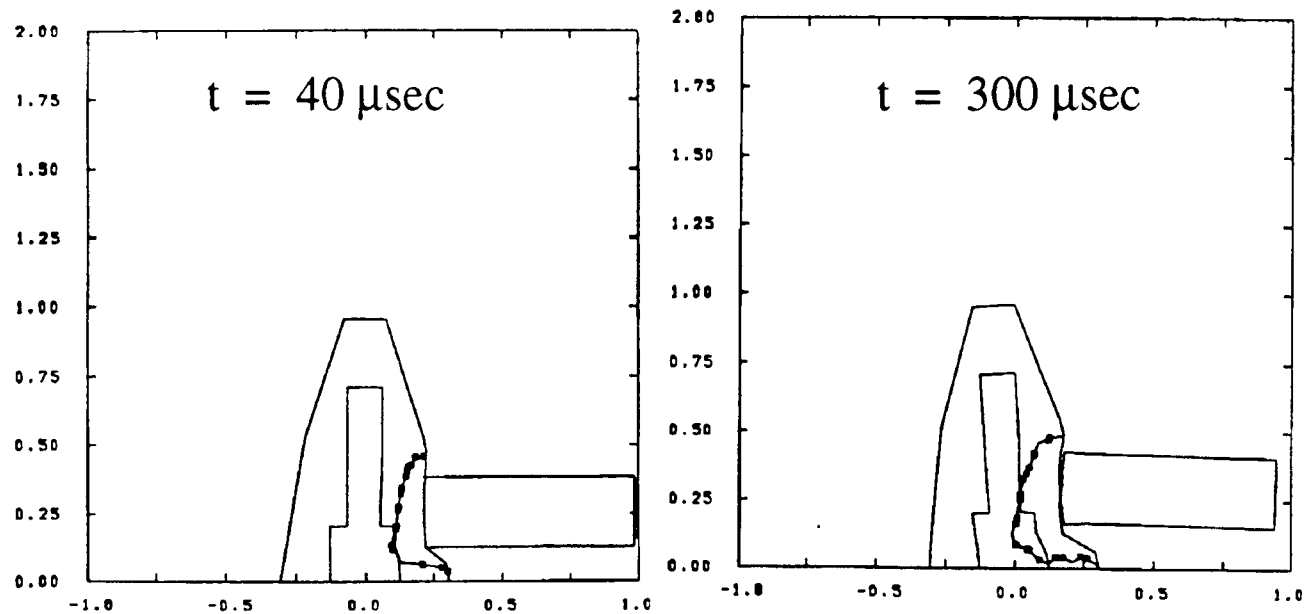


Figure 8. $\bar{\epsilon}^p = 0.20$ Contours for "Hard" Projectile Impacts a) Event 2, b) Event 3.

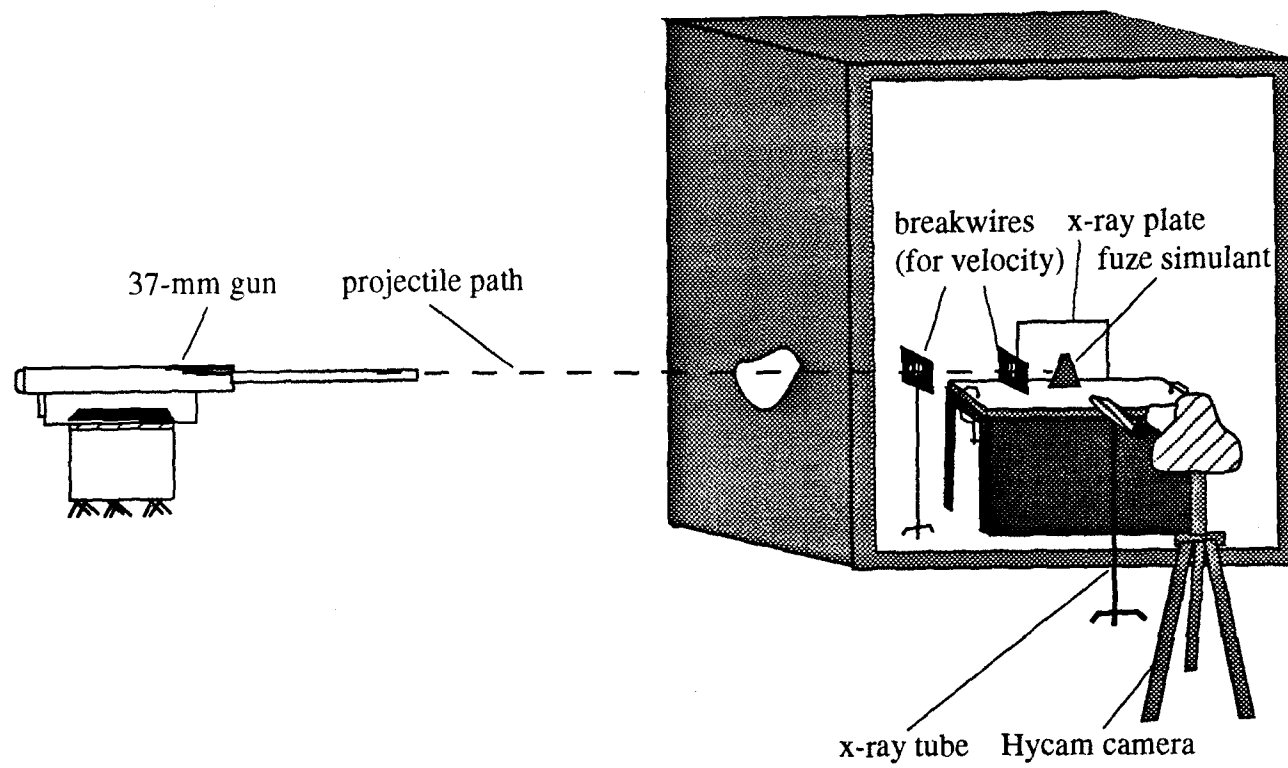


Figure 9. Ballistic Range Configuration.

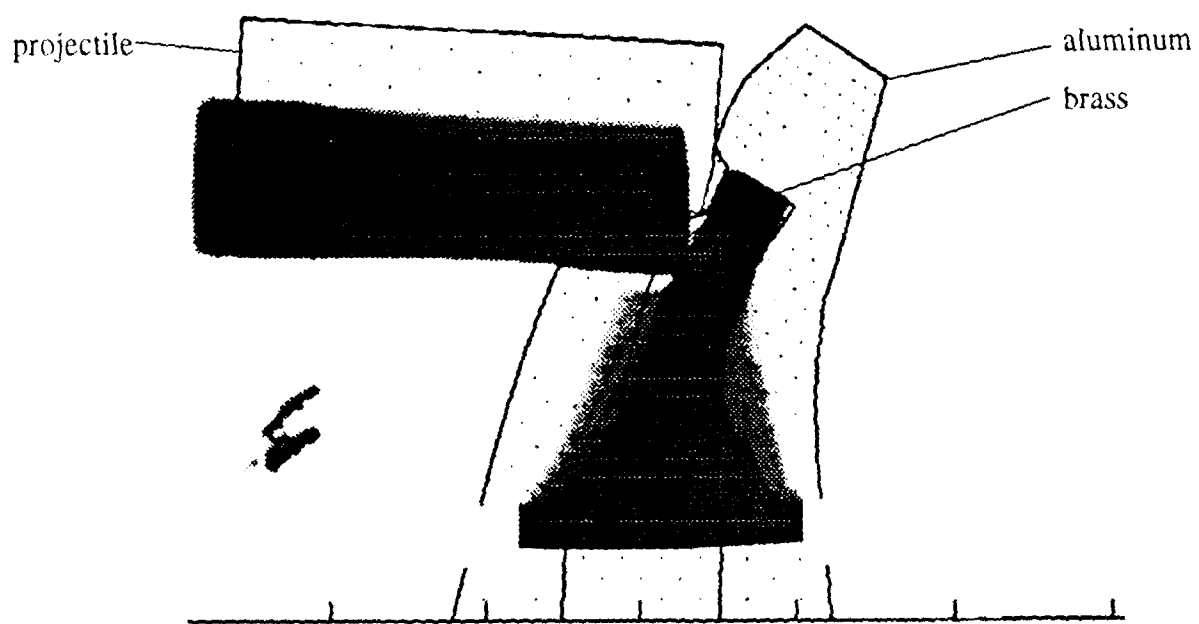


Figure 10. X-ray Radiograph of Impact Event at 272 μ s and EPIC92 Hydrocode Simulation Overlay at 280 μ s. Experimental Projectile Impact Point Is 0.27 in Below Simulation Impact Point.

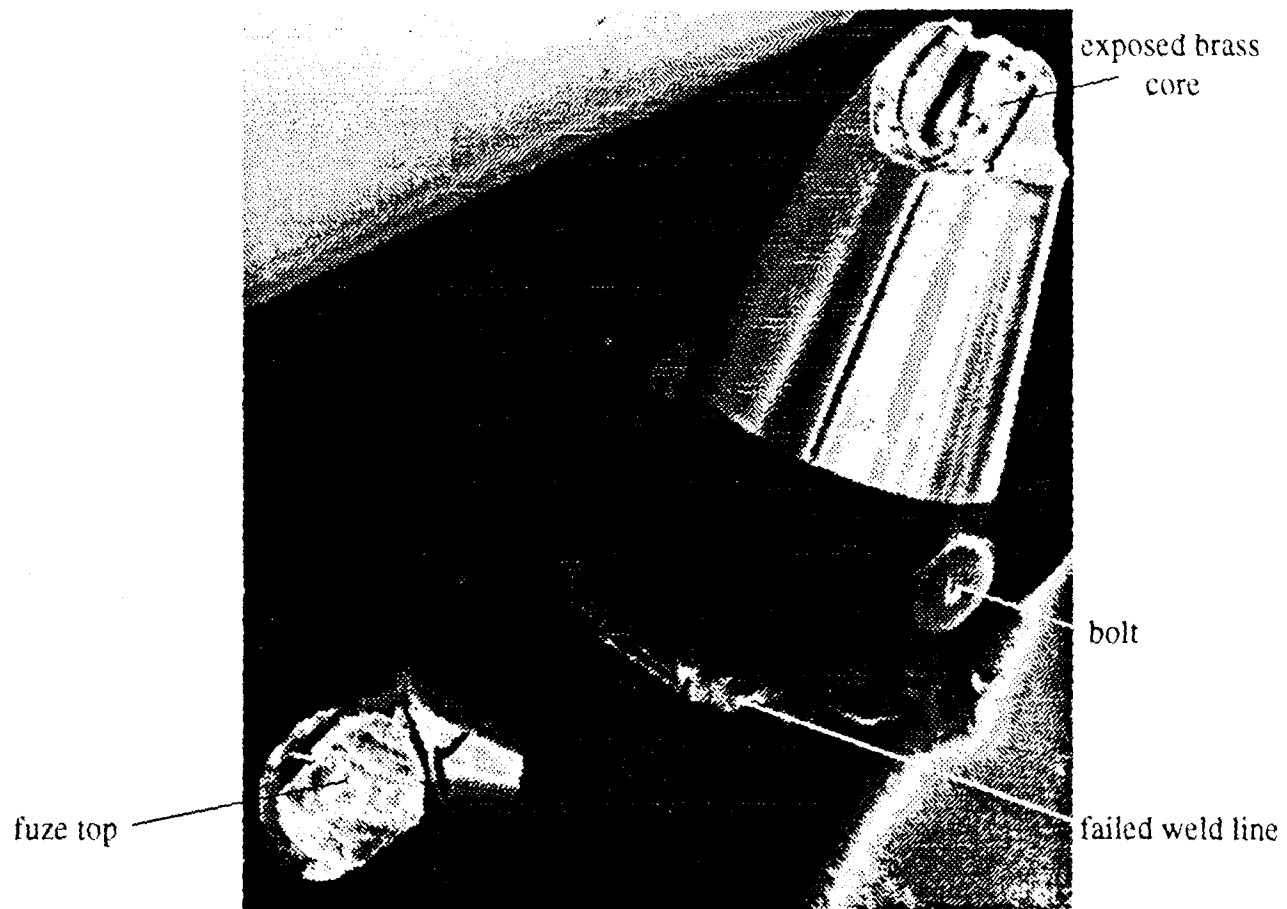


Figure 11. Photograph of Damaged Fuze Simulant Showing Severed Fuze Top with Circular Imprint of Projectile.

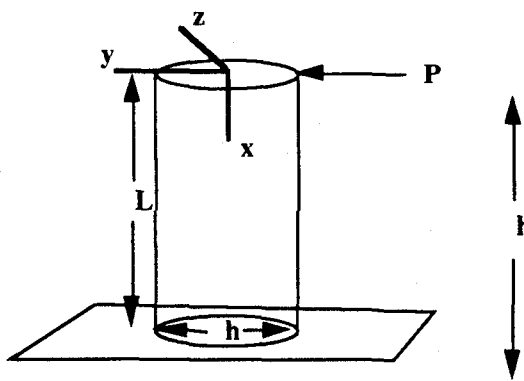


Figure 12a

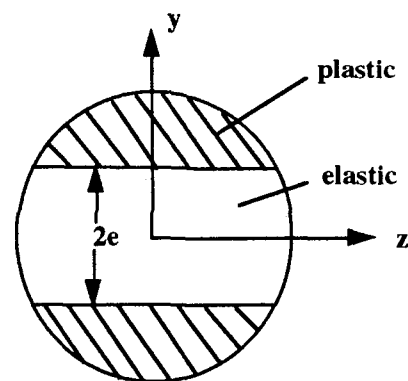


Figure 12b

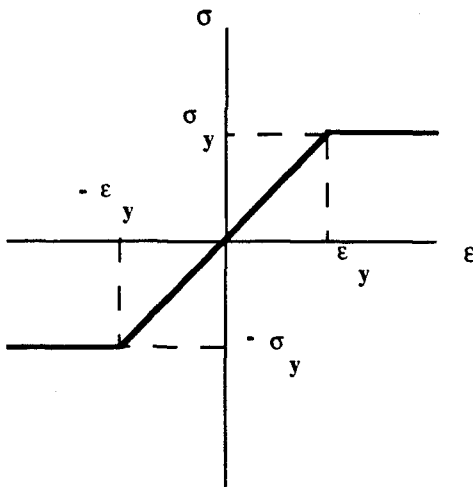


Figure 12c

Figure 12. Modeling Simplifications a) Simplified Fuze Geometry (Prismatic Circular Cantilever Beam), b) Beam Cross Section Showing Integration Coordinate System and Regions of Elastic and Plastic Behavior, c) Elastic-Perfectly Plastic Material Model.

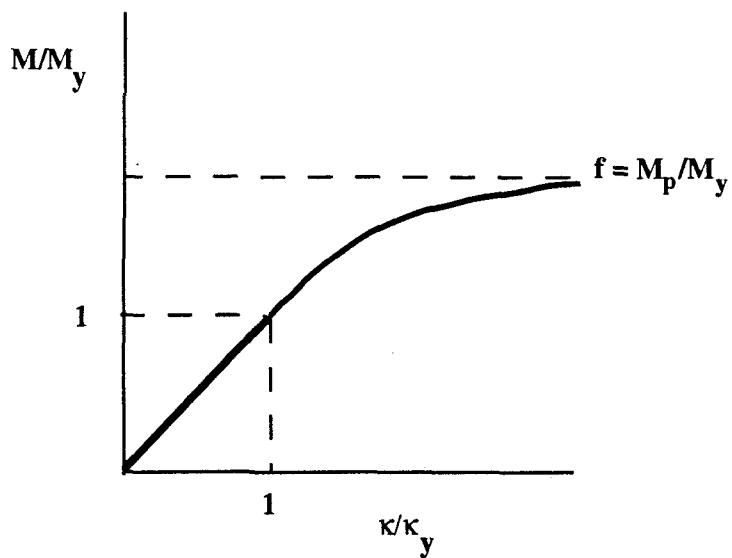


Figure 13. Moment Versus Curvature Relationship for an Elastic-Plastic Cantilever Beam.

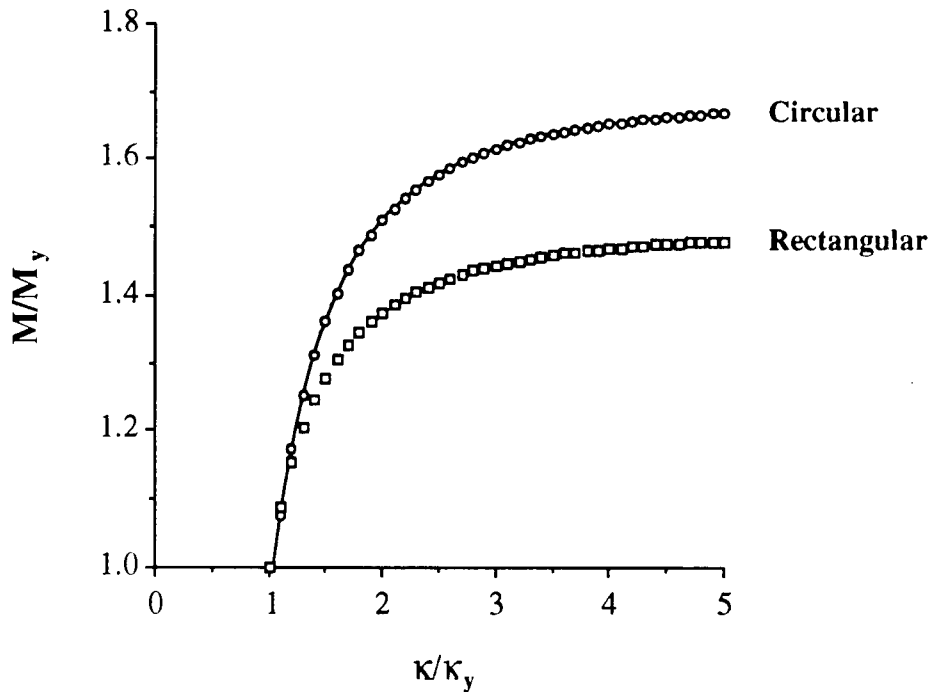


Figure 14. Moment Versus Curvature Plots for an Elastic-Plastic Cantilever Beam of Circular Cross Section. The Solid Line Is the Exact Solution (Eqn. 19), and the Circles Represent the Approximate Solution for κ/κ_y (Eqn. 22) Determined Using a Marquardt-Levenberg Algorithm. The Exact Solution for the Rectangular Beam (Eqn 20) Is Also Shown.

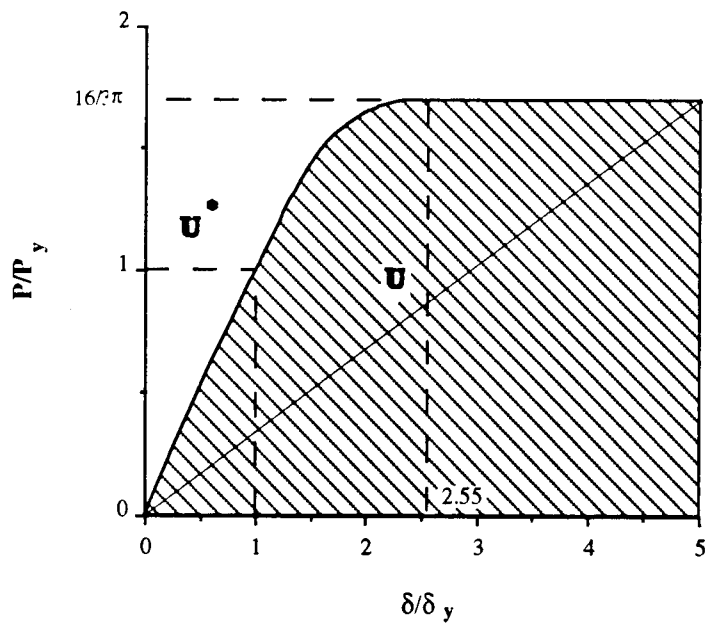


Figure 15. Load Versus Deflection (Eqn. 24) for an Elastic-Plastic Cantilever Beam of Circular Cross Section. U^* is the Complementary Energy (Eqn. 26) and U is Strain Energy (Eqn. 27) for the Beam Subjected to End Load P .

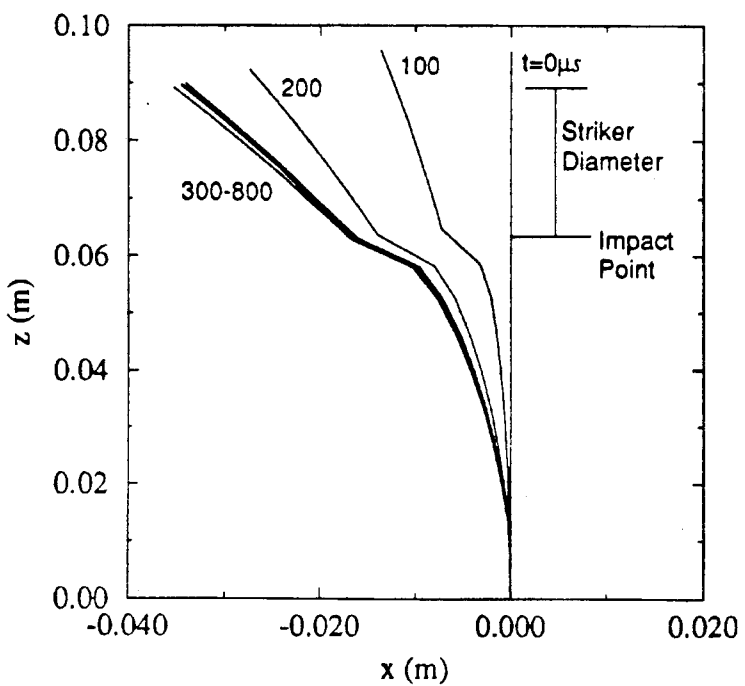


Figure 16. Fuze Centerline Distortion (in meters) Versus Time for Event 2. The Projectile Begins to Rebound at $\sim 360 \mu\text{s}$ and Separates from Fuze at $\sim 500 \mu\text{s}$.

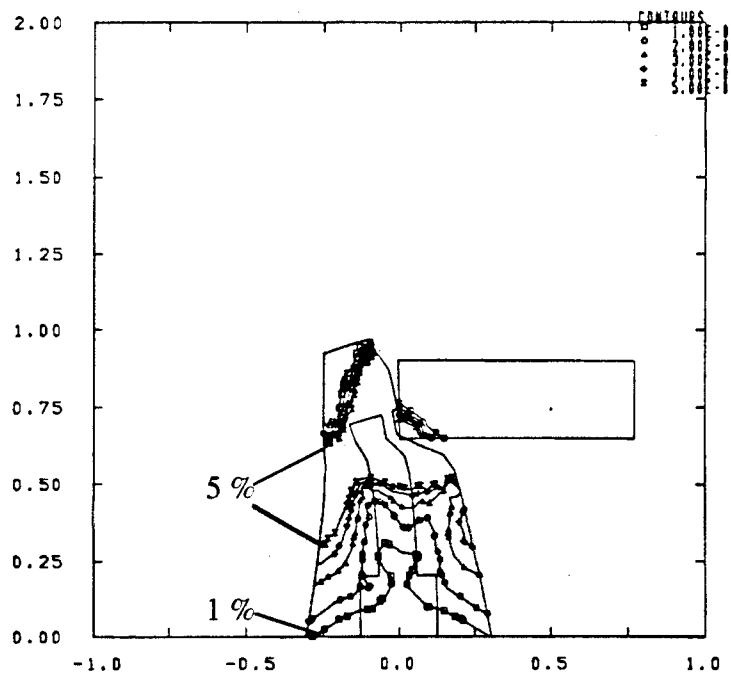


Figure 17. Equivalent Plastic Strain Contours at $120 \mu\text{s}$. Showing Fully Developed Plasticity Across the Diameter of the Fuze. Strain Increments are at 1% Through 5%.

INTENTIONALLY LEFT BLANK.

10. REFERENCES

Drucker, D. C. "The Effect of Shear on the Plastic Bending of Beams." Journal of Applied Mechanics, vol. 23, pp. 509-514, 1956.

Green, A. P. "A Theory of the Plastic Yielding Due to Bending of Cantilevers and Beams. Part II." Journal of the Mechanics and Physics of Solids, vol. 8, pp. 148-155, 1954.

Hallquist, J. O., and D. J. Benson. "DYNA3D User's Manual." UCID-19592, rev. 2, Lawrence Livermore National Laboratory, Livermore, CA, 1986.

Hodge Jr., P. G. "Interaction Curves for Shear and Bending of Plastic Beams." Journal of Applied Mechanics, vol. 24, pp. 453-456, 1957.

Holian, K. S., S. J. Mosso, D. A. Mandel, and R. Henninger. "MESA: A 3-D Computer Code for Armor/Anti-Armor Applications." LA-UR-91-569, Los Alamos National Laboratory Report, Los Alamos, NM, 1991.

Ingraffea, A. R. "Theory of Crack Initiation and Propagation in Rock." In: Fracture Mechanics of Rock. Edited by B. K. Atkinson. New York: Academic Press, pp. 71-110, 1989.

Johnson, G. R. "High Velocity Impact Calculations in Three Dimensions." Journal of Applied Mechanics, vol. 99, no. 1, pp. 95-100, 1977.

Johnson, G. R., and W. H. Cook. "Fracture Characteristics of Three Metals Subjected to Various Strains, Strain Rates, Temperatures and Pressures." Engineering Fracture Mechanics, vol. 21, no. 1, pp. 31-48, 1985.

Johnson, G. R., R. A. Stryk, D. E. Pratt, and J. A. Schonhardt. EPIC Hydrocode User's Workshop. Alliant Techsystems, Inc., Brooklyn Park, MN, October 1992a.

Johnson, G. R., R. A. Stryk, D. E. Pratt, and J. A. Schonhardt. User Instructions for the 1992 Version of the EPIC Code. Alliant Techsystems, Inc., Brooklyn Park, MN, October 1992b.

Jones, H. D., and F. J. Zerilli. "Reaction Kinetics of Metallized Explosives." Proceedings of the Materials Research Society Symposium, Structures and Properties of Energetic Materials, vol. 296, pp. 311-315, 1993.

Keer, L. M., and W. P. Schonberg. "Smooth Indentation of an Isotropic Cantilever Beam." International Journal of Solids and Structures, vol. 22, no. 1, pp. 87-106, 1986.

Lee, E. H., and P. S. Symonds. "Large Plastic Deformations of Beams Under Transverse Impact." Journal of Applied Mechanics, vol. 19, pp. 308-314, 1952.

Matuska, D. A. "HULL User's Manual." Air Force Armament Laboratory Report AD-A145000, Orlando Technology, Inc., Shalimar, FL, June 1984.

McGlaun, J. M., F. J. Zeigler, and S. L. Thompson. "CTH: A Three-Dimensional, Large Deformation, Shock Wave Physics Code." SAND 87-0726C, Sandia National Laboratory, Albuquerque, NM, 1987.

Monaghan, J. J. "Why Particle Methods Work." SIAM Journal of Science, Statistics and Computing, vol. 3, pp. 422-433, 1982.

Oberg, E., F. D. Jones, and H. L. Horton. Machinery's Handbook. Edited by H.H. Ryffel. New York: Industrial Press, 1984.

Parkes, E. W. "The Permanent Deformation of a Cantilever Struck Transversely at its Tip." Proceedings of the Royal Society of London, A228, pp. 462-476, 1955.

Patel, A., and R. Gold. Personal communication. U.S. Army Research Laboratory, Aberdeen Proving Ground, MD, October 1993.

Press, W. H., B. P. Flannery, S. A. Teukolsky, and W. T. Vetterling. Numerical Recipes-The Art of Scientific Computing. New York: Cambridge University Press, 1986.

Segletes, S. B. "Mechanisms Inducing Jet Rotation in Shear-Formed Shaped-Charge Liners." BRL-TR-3090, U.S. Army Ballistic Research Laboratory, Aberdeen Proving Ground, Maryland, March 1990.

Shu, D., W. J. Stronge, and T. X. Yu. "Oblique Impact at the Tip of a Cantilever." International Journal of Impact Engineering, vol. 12, no. 1, pp. 37-42, 1992.

Timoshenko, S. P., and J. M. Gere. Mechanics of Materials. New York: D. Van Nostrand Co., 1972.

Ting, T. C. T. "The Plastic Deformation of a Cantilever Beam with Strain-Rate Sensitivity Under Impulsive Loading." Journal of Applied Mechanics, vol. 31, pp. 38-42, 1964.

Ting, T. C. T. "Large Deformation of a Rigid, Ideally Plastic Cantilever Beam." Journal of Applied Mechanics, vol. 32, pp. 295-302, 1965.

Tipton, R. "CALE User's Manual," version 910701, Lawrence Livermore National Laboratory, 1991.

Zienkiewicz, O .C. The Finite Element Method. New York: McGraw-Hill Book Co., 1977.

LIST OF SYMBOLS

D	EPIC damage parameter
dA	beam area increment
D_{ijkl}	elastic modulus tensor
E	Young's modulus
e	limit of elastic behavior
h	beam diameter
h_s	tapered beam diameter at tip
h_b	tapered beam diameter at built-in end
I	beam moment of inertia
L	beam length
M	beam moment
M_y	beam yield moment
M_p	beam plastic moment
P	load
P_y	load at initial yield
T	homologous temperature
U	dimensionless strain energy
U^*	dimensionless complementary energy
U_{Tot}	total dimensionless strain energy
v	elastic beam deflection
v_{max}	maximum elastic tip deflection
x	beam axial coordinate
x_e	limit of elastic behavior
y	beam coordinate
δ	beam tip deflection
δ_y	tip deflection at initial yield
$d\sigma_{kl}$	incremental stress tensor
$d\epsilon_{ij}$	incremental strain tensor
$d\epsilon_{ij}^p$	incremental plastic strain tensor
$\dot{\epsilon}$	strain rate
$\dot{\epsilon}_0$	normalization strain rate
$\dot{\epsilon}^*$	dimensionless plastic strain rate
ϵ^f	fracture strain

$\bar{\epsilon}^p$ equivalent plastic strain
 $\Delta\bar{\epsilon}^p$ incremental equivalent plastic strain
 κ beam curvature
 κ_y beam curvature at initial yield
 σ beam stress
 $\bar{\sigma}$ equivalent stress
 σ^* pressure-stress ratio
 σ_m mean normal stress
 σ_{max} maximum beam stress
 σ_b maximum bending stress
 σ'_{ij} deviatoric stress

<u>NO. OF COPIES</u>	<u>ORGANIZATION</u>	<u>NO. OF COPIES</u>	<u>ORGANIZATION</u>
2	ADMINISTRATOR DTIC ATTN DTIC DDA CAMERON STATION ALEXANDRIA VA 22304-6145	1	DIR USA TRADOC ANALYSIS CMD ATTN ATRC WSR WSMR NM 88002-5502
1	CDR USAMC ATTN AMCAM 5001 EISENHOWER AVE ALEXANDRIA VA 22333-0001	1	CMDT US ARMY INFANTRY SCHOOL ATTN ATSH CD SECURITY MGR FT BENNING GA 31905-5660
1	DIR USARL ATTN AMSRL OP SD TA 2800 POWDER MILL RD ADELPHI MD 20783-1145		<u>ABERDEEN PROVING GROUND</u>
3	DIR USARL ATTN AMSRL OP SD TL 2800 POWDER MILL RD ADELPHI MD 20783-1145	2	DIR USAMSA ATTN AMXSY D AMXSY MP H COHEN
1	DIR USARL ATTN AMSRL OP SD TP 2800 POWDER MILL RD ADELPHI MD 20783-1145	1	CDR USATECOM ATTN AMSTE TC
2	CDR US ARMY ARDEC ATTN SMCAR TDC PCTNY ARSXL NJ 07806-5000	1	DIR USAERDEC ATTN SCBRD RT
1	DIR BENET LABS ATTN SMCAR CCB TL WATERVLIET NY 12189-4050	1	CDR USACBDCOM ATTN AMSCB CII
1	DIR USA ADVANCED SYSTEMS R&A OFC ATTN AMSAT R NR MS 219 1 AMES RESEARCH CENTER MOFFETT FLD CA 94035-1000	5	DIR USARL ATTN AMSRL OP AP L
1	CDR US ARMY MICOM ATTN AMSMI RD CS R DOC RDSTN ARSXL AL 35898-5010		
1	CDR US ARMY TACOM ATTN AMSTA JSK ARMOR ENG BR WARREN MI 48397-5000		

<u>NO. OF COPIES</u>	<u>ORGANIZATION</u>	<u>NO. OF COPIES</u>	<u>ORGANIZATION</u>
1	HQDA SARD TT DR F MILTON WASH DC 20310-0103	5	CDR US ARMY ARDEC ATTN SMCAR CCH T S MUSALLI P CHRISTIAN K FEHSAL N KRASNOW R CARR PCTNY ARSRL NJ 07806-5000
1	HQDA SARD TT MR J APPEL WASH DC 20310-0103	1	CDR US ARMY ARDEC ATTN SMCAR CCH V E FENNELL PCTNY ARSRL NJ 07806-5000
1	HQDA SARD TT MS C NASH WASH DC 20310-0103	1	CDR US ARMY ARDEC ATTN SMCAR CCH J DELORENZO PCTNY ARSRL NJ 07806-5000
1	HQDA SARD TR DR R CHAIT WASH DC 20310-0103	2	CDR US ARMY ARDEC ATTN SMCAR CC J HEDDERICH COL SINCLAIR PCTNY ARSRL NJ 07806-5000
1	HQDA SARD TR MS K KOMINOS WASH DC 20310-0103	1	CDR US ARMY ARDEC ATTN SMCAR CCH P J LUTZ PCTNY ARSRL NJ 07806-5000
1	DIR USARL ATTN AMSRL CP CA D SNIDER 2800 POWDER MILL ROAD ADELPHI MD 20783-1145	2	CDR US ARMY ARDEC ATTN SMCAR FSA M D DEMELLA F DIORIO PCTNY ARSRL NJ 07806-5000
8	DIR USARL ATTN AMSRL MA P L JOHNSON B HALPIN T CHOU C WHITE J MCLAUGHLIN AMSRL MA PA D GRANVILLE W HASKELL AMSRL MA MA G HAGNAUER WATERTOWN MA 02172-0001	1	CDR US ARMY ARDEC ATTN SMCAR FSA C SPINELLI PCTNY ARSRL NJ 07806-5000
4	CDR US ARMY ARDEC ATTN SMCAR FSE T GORA E ANDRICOPOULOS B KNUTELSKY A GRAF PCTNY ARSRL NJ 07806-5000	11	DIR BENET LABS ATTN SMCAR CCB C KITCHENS J KEANE J SANTINI J VASILAKIS G FRIAR R FISCELLA V MONTVORI J WRZOCHALSKI J BATTAGLIA R HASENBEIN SMCAR CCB R S SOPOK WATERVLIET NY 12189
3	CDR US ARMY ARDEC ATTN SMCAR TD R PRICE V LINDER T DAVIDSON PCTNY ARSRL NJ 07806-5000		
1	CDR US ARMY ARDEC ATTN F MCLAUGHLIN PCTNY ARSRL NJ 07806-5000		

<u>NO. OF COPIES</u>	<u>ORGANIZATION</u>	<u>NO. OF COPIES</u>	<u>ORGANIZATION</u>
1	CDR WATERVLIET ARSENAL ATTN SMCWV QAE Q C HOWD BLDG 44 WATERVLIET NY 12189-4050	2	US ARMY RESEARCH OFFICE ENGINEERING SCIENCES DIV ATTN G ANDERSON R SINGLETON PO BOX 12211 RSCH TRI PK NC 27709-2211
1	CDR WATERVLIET ARSENAL ATTN SMCWV SPM T MCCLOSKEY BLDG 25 3 WATERVLIET NY 12189-4050	2	PM SADARM PCTNY ARSRL NJ 07806-5000
1	CDR WATERVLIET ARSENAL ATTN SMCWV QA QS K INSCO WATERVLIET NY 12189-4050	2	PM TMAS ATTN SFAE AR TMA COL BREGARD C KIMKER PCTNY ARSRL NJ 07806-5000
1	CDR PRODUCTION BASE MODERNIZATION ACTIVITY ATTN AMSMC PBM K PCTNY ARSRL NJ 07806-5000	3	PM TMAS ATTN SFAE AR TMA MD H YUEN J MCGREEN R KOWALSKI PCTNY ARSRL NJ 07806-5000
1	CDR USABRDC ATTN STRBE JBC C KOMINOS FT BELVOIR VA 22060-5606	2	PM TMAS ATTN SFAE AR TMA MS R JOINSON D GUZIEWICZ PCTNY ARSRL NJ 07806-5000
1	DIR USACRREL ATTN P DUTTA 72 LYME ROAD HANOVER NH 03755	1	PM TMAS ATTN SFAE AR TMA MP W LANG PCTNY ARSRL NJ 07806-5000
1	DIR USARL ATTN AMSRL WT L D WOODBURY 2800 POWDER MILL ROAD ADELPHI MD 20783-1145	2	PEO ARMAMENTS ATTN SFAE AR PM D ADAMS T MCWILLIAMS PCTNY ARSRL NJ 07806-5000
4	CDR US ARMY MICOM ATTN AMSMI RD W MCCORKLE AMSMI RD ST P DOYLE AMSMI RD ST CN T VANDIVER AMSMI RD ST WF MIKE COLE RDSTN ARSRL AL 35898	1	PEO FIELD ARTILLERY SYSTEMS ATTN SFAE FAS PM H GOLDMAN PCTNY ARSRL NJ 07806-5000
2	US ARMY RESEARCH OFFICE MATH & COMPUTER SCIENCES DIV ATTN ANDREW CROWSON J CHANDRA PO BOX 12211 RSCH TRI PK NC 27709-2211	4	PM AFAS ATTN LTC D ELLIS G DELCOCO J SHIELDS B MACHAK PCTNY ARSRL NJ 07806-5000

<u>NO. OF COPIES</u>	<u>ORGANIZATION</u>	<u>NO. OF COPIES</u>	<u>ORGANIZATION</u>
2	CDR WRIGHT PATTERSON AFB ATTN WL MLBM S DONALDSON WL FIV A MAYER DAYTON OH 45433-7750	1	OAK RIDGE NATIONAL LAB ATTN R M DAVIS PO BOX 2008 OAK RIDGE TN 37831-6195
2	NASA Langley RSCH CTR MAIL STOP 266 ATTN AMSRL VS W ELBER AMSRL VS S F BARTLETT JR HAMPTON VA 23681-0001	2	BATTELLE PNL ATTN M SMITH M C C BAMPTON PO BOX 999 RICHLAND WA 99352
2	NAVAL SURFACE WARFARE CTR CODE G33 DAHLGREN VA 22448	6	DIR SNL ATTN C ROBINSON G BENEDETTI W KAWAHARA K PERANO D DAWSON P NIELAN PO BOX 969 LIVERMORE CA 94550-0096
1	OFFICE OF NAVAL RESEARCH MECH DIV CODE 1132SM ATTN YAPA RAJAPAKSE ARLINGTON VA 22217	1	PENN STATE UNIV ATTN RICHARD MCNITT 227 HAMMOND BLDG UNIVERSITY PARK PA 16802
1	NAVAL ORDNANCE STATION ADV SYS TECHNOLOGY BR ATTN D HOLMES CODE 2011 LOUISVILLE KY 40214-5245	1	SOUTHWEST RSCH INSTITUTE ATTN C ANDERSON 6220 CULEBRA ROAD SAN ANTONIO TX 78284
1	DAVID TAYLOR RSCH CTR SHIP STRCTS & PRTCTN DEPT ATTN J CORRADO CODE 1702 BETHESDA MD 20084	1	UCLA MANE DEPT ENGRG IV ATTN H THOMAS HAHN LOS ANGELES CA 90024-1597
2	DAVID TAYLOR RSCH CTR ATTN R ROCKWELL W PHYILLAER BETHESDA MD 20054-5000	2	UNIV OF DAYTON RSCH INST ATTN RAN Y KIM AJIT K ROY 300 COLLEGE PARK AVE DAYTON OH 45469-0168
5	DIR LLNL ATTN R CHRISTENSEN S DETERESA W FENG F MAGNESS M FINGER PO BOX 808 LIVERMORE CA 94550	2	UNIV OF DELAWARE CTR FOR COMPOSITE MTRLS ATTN J GILLESPE M SANTARE 201 SPENCER LABORATORY NEWARK DE 19716
1	DIR LANL ATTN D RABERN MEE 13 MAIL STOP J 576 PO BOX 1633 LOS ALAMOS NM 87545		

<u>NO. OF COPIES</u>	<u>ORGANIZATION</u>	<u>NO. OF COPIES</u>	<u>ORGANIZATION</u>
1	UNIV OF TEXAS AT AUSTIN CTR FOR ELECTROMECHANICS ATTN J PRICE 10100 BURNET ROAD AUSTIN TX 78758-4497	1	CUSTOM ANALYTICAL ENGRNG SYSTEMS INC ATTN A ALEXANDER STAR ROUTE BOX 4A FLINTSTONE MD 21530
1	AAI CORPORATION ATTN TECH LIBRARY PO BOX 126 HUNT VALLEY MD 21030-0126	1	GDLS DIVISION ATTN D BARTLE PO BOX 1901 WARREN MI 48090
1	ARMTEC DEFENSE PRODUCTS ATTN STEVE DYER PO BOX 848 COACHELLA CA 92236	3	HERCULES INCORPORATED ATTN G KUEBEKER J VERMEYCHUK B MANDERVILLE JR HERCULES PLAZA WILMINGTON DE 19894
3	ALLIANT TECHSYSTEMS INC ATTN J BODE C CANDLAND K WARD 5901 LINCOLN DR MINNEAPOLIS MN 55346-1674	1	HEXCEL ATTN M SHELENDICH PO BOX 2312 DUBLIN CA 94568-0705
1	ALLIANT TECHSYSTEMS INC ATTN TIM HOLMQUIST 600 SECOND STREET NE HOPKINS MN 55343	1	IAP RESEARCH INC ATTN A CHALLITA 2763 CULVER AVENUE DAYTON OHIO 45429
1	BALLISTIC IMPACT DYNAMICS ATTN RODNEY RECHT 3650 S CHEROKEE 2 ENGLEWOOD CO 80110	5	INSTITUTE FOR ADVANCED TECHNOLOGY ATTN T KIEHNE H FAIR P SULLIVAN S BLESS R SUBRAMANIAN 4030 2 W BRAKER LANE AUSTIN TX 78759
1	CALIFORNIA RSRCH & TECH ATTN DENNIS ORPHAL 5117 JOHNSON DRIVE PLEASANTON CA 94566	1	INTERFEROMETRICS INC ATTN R LARRIVA VP 8150 LEESBURG PIKE VIENNA VA 22100
1	CHAMBERLAIN MFG CORP R&D DIVISION ATTN M TOWNSEND PO BOX 2545 WATERLOO IA 50704	3	KAMAN SCIENCES CORP ATTN D ELDER T HAYDEN N ARI PO BOX 7463 COLORADO SPRINGS CO 80933
1	COMP MECHANICS ASSOC ATTN JONAS A ZUKAS PO BOX 11314 BALTIMORE MD 21239-0314		

<u>NO. OF COPIES</u>	<u>ORGANIZATION</u>	<u>NO. OF COPIES</u>	<u>ORGANIZATION</u>
1	D R KENNEDY & ASSOC INC ATTN D KENNEDY PO BOX 4003 MOUNTAIN VIEW CA 94040	109	<u>ABERDEEN PROVING GROUND</u> DIR USARL ATTN AMSRL CI C MERMAGEN 394 AMSRL CI C W STUREK 1121 AMSRL CI CB R KASTE 394 AMSRL CI S A MARK 309 AMSRL SL B P DEITZ 328 AMSRL SL BA J WALBERT 1065 AMSRL SL BL D BELY 328 AMSRL SL I D HASKILL 1065 AMSRL WT P A HORST 390A AMSRL WT PA T MINOR 390 C LEVERITT 390 D KOOKER 390A
1	LIVERMORE SOFTWARE TECH CORP ATTN J O HALLQUIST 2876 WAVERLY WAY LIVERMORE CA 94550		AMSRL WT PB E SCHMIDT 120 P PLOSTINS 120
2	LORAL VOUGHT SYS CORP ATTN G JACKSON K COOK 1701 WEST MARSHALL DR GRAND PRAIRIE TX 75051		AMSRL WT PC R FIFER 390A AMSRL WT PD B BURNS 390 W DRYSDALE 390 K BANNISTER 390 T BOGETTI 390 J BENDER 390 R MURRAY 390 R KIRKENDALL 390
1	LORAL VOUGHT SYS CORP ATTN KEN HAVENS MS EM 36 PO BOX 650003 DALLAS TX 75265-0003		T ERLINE 390 D HOPKINS 390 S WILKERSON 390 C MCCALL 390 D HENRY 390 R KASTE 390 L BURTON 390
2	MARTIN MARIETTA CORP ATTN P DEWAR L SPONAR 230 EAST GODDARD BLVD KING OF PRUSSIA PA 19406		J TZENG 390 R LIEB 390 G GAZONAS 390 5 CP M LEADORE 390
2	OLIN CORPORATION FLINCHBAUGH DIV ATTN E STEINER B STEWART PO BOX 127 RED LION PA 17356		AMSRL WT PD ALC A ABRAHAMIAN K BARNES M BERMAN H DAVISON A FRYDMAN T LI W MCINTOSH E SZYMANSKI
1	OLIN CORPORATION ATTN L WHITMORE 10101 9TH ST NORTH ST PETERSBURG FL 33702		
2	UNIV OF MINNESOTA AHPCRC ATTN G SELL D AUSTIN 1100 WASHINGTON AVE S MINNEAPOLIS MN 55415		

NO. OF
COPIES ORGANIZATION

AMSLR WT T
W MORRISON 309
T WRIGHT 309

AMSLR WT TA
W GILLICH 390
W BRUCHEY 390
J DEHN 390

AMSLR WT TB
K BENJAMIN 309
T DORSEY 309
R FREY 309
F GREGORY 309

W HILLSTROM 309
W LAWRENCE 309
O LYMAN 1185
J STARKENBERG 309
L VANDE KIEFT 309
J WATSON 309
V BOYLE 309 5 CP

S STEGALL 1185 5 CP
AMSLR WT TC
W DE ROSSET 309
K KIMSEY 309
R COATES 309
F GRACE 309
M LAMPSON 309
D SCHEFFLER 309
B SORENSEN 309
R SUMMERS 309
E WALKER 309
W WALTERS 309

AMSLR WT TD
D DIETRICH 309
G RANDERS PEHRSON 309
J HUFFINGTON 309
A DAS GUPTA 309
J SANTIAGO 309
K FRANK
J HARRISON
M SCHEIDLER
S SEGLETES 5 CP
J WALTER

AMSLR WT NC
R LOTTERO 309
R PEARSON 309
S SCHRAML 309

AMSLR WT W C MURPHY 120

AMSLR WT WA
H ROGERS 394
B MOORE 394
A BARAN 394

NO. OF
COPIES ORGANIZATION

AMSLR WT WB
F BRANDON 120
W D'AMICO 120

AMSLR WT WC J ROCCHIO 120

AMSLR WT WD
A ZIELINSKI 120
J POWELL 120
A PRAKASH 120
AMSLR WT WE
J TEMPERLEY 120

J THOMAS 394

INTENTIONALLY LEFT BLANK.

USER EVALUATION SHEET/CHANGE OF ADDRESS

This Laboratory undertakes a continuing effort to improve the quality of the reports it publishes. Your comments/answers to the items/questions below will aid us in our efforts.

1. ARL Report Number ARL-TR-665 Date of Report January 1995

2. Date Report Received _____

3. Does this report satisfy a need? (Comment on purpose, related project, or other area of interest for which the report will be used.)

4. Specifically, how is the report being used? (Information source, design data, procedure, source of ideas, etc.)

5. Has the information in this report led to any quantitative savings as far as man-hours or dollars saved, operating costs avoided, or efficiencies achieved, etc? If so, please elaborate.

6. General Comments. What do you think should be changed to improve future reports? (Indicate changes to organization, technical content, format, etc.)

Organization _____

CURRENT
ADDRESS

Name _____

Street or P.O. Box No. _____

City, State, Zip Code _____

7. If indicating a Change of Address or Address Correction, please provide the Current or Correct address above and the Old or Incorrect address below.

Organization _____

OLD
ADDRESS

Name _____

Street or P.O. Box No. _____

City, State, Zip Code _____

(Remove this sheet, fold as indicated, tape closed, and mail.)
(DO NOT STAPLE)

DEPARTMENT OF THE ARMY

OFFICIAL BUSINESS

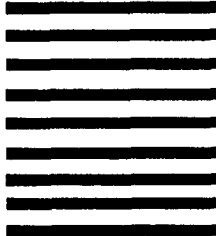


NO POSTAGE
NECESSARY
IF MAILED
IN THE
UNITED STATES

BUSINESS REPLY MAIL
FIRST CLASS PERMIT NO 0001, APG, MD

Postage will be paid by addressee

Director
U.S. Army Research Laboratory
ATTN: AMSRL-OP-AP-L
Aberdeen Proving Ground, MD 21005-5066

A series of eight thick horizontal lines of varying lengths, used for postal sorting.